UNIVERSITY OF CALIFORNIA
SANTA CRUZ

WIDE-FIELD KINEMATIC STRUCTURE OF EARLY-TYPE GALAXY HALOS

A dissertation submitted in partial satisfaction of the
requirements for the degree of

DOCTOR OF PHILOSOPHY

in

ASTRONOMY AND ASTROPHYSICS

by

Jacob Antony Arnold

June 2013

The Dissertation of Jacob Antony Arnold
is approved:

Professor Jean Brodie, Chair

Professor Raja Guha Thakurta

Professor Aaron Romanowsky

Tyrus Miller
Vice Provost and Dean of Graduate Studies

Table of Contents

List of Figures

List of Tables

Abstract

Wide-Field Kinematic Structure of Early-Type Galaxy Halos

by

Jacob Antony Arnold

The stellar halos of nearby galaxies bare the signatures of the mass-assembly processes that have driven galaxy evolution over the last $\sim$10 Gyr. Finding and interpreting these relict clues in galaxies within and beyond the local group offers one of the most promising avenues for understanding how galaxies accumulate their stars over time. To tackle this problem we have performed a systematic study of the wide-field kinematic structure of nearby (D$<$ 30 Mpc) early-type galaxies (ETGs), based on two-dimensional absorption-line stellar spectroscopy out to several effective radii ($\sim 3\,R_e$). The 22 galaxies presented here span a range of environments (field, group, and cluster), intrinsic luminosities ($-22.4 < \mathrm{M_k} < -25.6$), and morphologies (S0-E0). The data consist of moderate resolution ($\delta\lambda \sim$60 km s^{-1}) integrated-stellar-light spectra extracted from the individual slitlets of custom Keck/DEIMOS slitmasks. The complicating effects of strong emission line features are avoided by targeting the spectral region surrounding the near-infrared Calcium II triplet. For each spectrum, we parameterize the line-of-sight velocity distribution (LOSVD) as a truncated Gauss-Hermite series convolved with an optimally weighted combination of stellar templates. These kinematic measurements (V, σ, h_3, and h_4) are combined with literature values to construct spatially resolved maps of large-scale kinematic structure. A variety of kinematic behaviors are observed beyond $\sim 1\,R_e$, potentially reflecting the stochastic and chaotic assembly of stellar bulges and halos in early-type galaxies.

Next, we describe a global analysis (out to $5\,R_e$) of kinematics and metallicity in the nearest S0 galaxy, NGC 3115, along with implications for its assembly history. The data include

high-quality wide-field imaging and multi-slit spectra of the field stars and globular clusters (GCs). Within two effective radii, the bulge (as traced by the stars and metal-rich GCs) is flattened and rotates rapidly. At larger radii, the rotation declines dramatically, while the characteristic GC metallicities also decrease with radius. We argue that this pattern is not naturally explained by a binary major merger, but instead by a two-phase assembly process where the inner regions have formed in an early violent, dissipative phase, followed by the protracted growth of the outer parts via minor mergers. To test this hypothesis and improve our understanding of the growth of stellar halos we compare our observational results to high-resolution cosmological galaxy simulations. We describe a methodology for visualizing these data and present our initial comparisons between theory and observation, which suggest that the aggregate effects of many minor mergers dictate the large-scale kinematic structure of present day ETGs.

Dedicated to

Mah Wiiiiiiiiiife.

Acknowledgments

I am incredibly grateful to my advisor Jean Brodie, who has given me the opportunity to use the world's greatest telescopes, to become utterly engrossed in scientific endeavor, and to follow my curiosity wherever it may lead. Her unwavering support, optimism, and kindness has made my time at UC Santa Cruz truly special, and I will forever be thankful for her guiding hand in helping me become an astronomer. I also want to thank my other advisor Aaron Romanowsky for his incredible guidance, patience, and generosity over the last six years. His unflagging enthusiasm for science, many brilliant ideas, and thoughtful suggestions have been both appreciated and admired. And of course, a special thanks to Raja Guha Thakurta for agreeing to be on my qualifying and thesis committees, and for his kindness, positivity, and helpful suggestions.

Many, many, many thanks to Ken Ostrowski for setting me on this path all those years ago, and for being an incredible friend and mentor. It is impossible to express how much his support over the years has meant to me. Much gratitude to my fellow graduate students for their friendship, kindness, and laughter. Their companionship during the many long-nights, stressful moments, and countless sighs have made this journey well worth it.

Finally, I must thank my incredibly amazing and brilliant wife and partner Autumn for her constant love and support.

Chapter 1

Introduction

The relict signatures of galactic mass assembly are evident in the internal dynamical structure of present day galaxies. Within the ΛCDM cosmological framework, the relevant assembly processes are largely hierarchical in nature. The expectation being that all galaxies grow through successive merger and accretion events, e.g., White & Rees (1978), with early-type galaxies (ETGs: ellipticals and S0s) experiencing somewhat more active assembly histories than later type galaxies. Consequently, ETGs should serve as natural locations to investigate the dynamical structure resulting from hierarchical galactic mass buildup.

Nearly four decades of detailed observations have shown that the galaxies comprising the ETG class are anything but the originally perceived simple featureless systems. While they are remarkably uniform in some respects, e.g., they follow strict scaling relations (Djorgovski & Davis 1987, Dressler et al. 1987), ETGs also exhibit a diversity of structural features and dynamical behaviors. For example, rapid to vanishing rotation (Illingworth 1977, Davies et al. 1983), boxy to disky isophotes (Bender et al. 1989), power-law or cored central surface brightness profiles (e.g., Lauer et al. 1995, Kormendy et al. 2009), and negligible to significant radio and X-ray luminosity (e.g., Bender et al. 1987; 1989). Because many of these properties are correlated

in elliptical galaxies (Bender et al. 1989, Nieto et al. 1991), they can, as a class, be sub-divided into two primary categories comprised of boxy and disky varieties (Kormendy & Bender 1996).

More recently, this ETG division has been extended to include S0s and recast in terms of projected stellar angular momentum (λ_{R_e}) within $\sim$1 R_e (Emsellem et al. 2007), or more precisely, in terms of λ_{R_e} and isophotal flattening (Emsellem et al. 2011). So called fast rotators (FRs) have larger λ_{R_e} values, are diskier, tend to have power-law central surface brightness profiles, and exhibit regular aligned rotation. These properties are all consistent with the idea that fast rotators are oblate axisymmetric, with a moderate amount of radial anisotropy (e.g., van der Marel 1991, Cappellari et al. 2007; cf., Kronawitter et al. 2000, Gebhardt et al. 2003). In contrast, slow rotators (SRs) have little net angular momentum within 1 R_e, are less flattened and boxier, tend to be more massive, have cored surface brightness profiles, and are more likely to exhibit kinematic twisting, misalignment, or kinematically decoupled cores. The semi-analytic model of Khochfar et al. (2011) suggests that mass assembly history plays a key role in establishing this kinematic division; with more and less merging activity being associated with slow and fast rotators respectively.

Mergers have long been invoked to explain the formation of ETGs, which is perhaps unsurprising today given their integral role in galaxy assembly within the concordance cosmology. This expectation has motivated a number of efforts to numerically simulate the remnants of binary major-mergers between disk galaxies (e.g., Hernquist 1992, Barnes 1992, Bendo & Barnes 2000, Burkert & Naab 2003, Bournaud et al. 2005, Cox et al. 2006, Hoffman et al. 2010, Chilingarian et al. 2010, Bois et al. 2011). Comparisons between simulated remnants and observations show generally good agreement in terms of isophote shape (Naab et al. 1999) and kinematic structure within 1 R_e (Jesseit et al. 2007). Variations in choice of merger parameters (e.g., mass ratio, gas content, orbital trajectory) can reproduce much of the observed diversity in ETG features (e.g., Bournaud et al. 2005, Cox et al. 2006, Hoffman et al. 2010).

However, an important drawback to idealized binary major-merger simulations is that they do not include the effects of a realistic cosmological accretion history (see chapter 4). Quite simply, minor mergers and accretion events should be far more common than major mergers (Stewart et al. 2008). The importance of this has been highlighted recently with the recognition that the strong size evolution of massive ETGs since $z \approx 2-3$ (e.g., Daddi et al. 2005, Cimatti et al. 2008, Dokkum et al. 2008) may be driven by minor-mergers (Naab et al. 2009, Bezanson et al. 2009, Oser et al. 2010). The emergent picture includes two distinct phases of ETG growth. The first phase involves the formation of a compact ($\approx$ 1kpc) in-situ bulge at $z > 2$, likely the result of violent dissipative events such as a gas rich major-merger or a fragmenting turbulent disk fed by cold flows (e.g., Noguchi 1999, Elmegreen et al. 2008, Dekel et al. 2009, Ceverino et al. 2010). The second phase is slower, taking place between $0 < z < 3$ (Oser et al. 2011), and consists of mostly dry minor mergers which serve to increase the size of the galaxy (see e.g., van Dokkum et al. 2010, Newman et al. 2012).

In this view, nearby ETGs are layered structures. The central regions being the remnants of those compact in-situ bulges formed at $z > 2$, and the outer extended halos consisting of predominantly accreted material from disrupted satellites. At intermediate radii there is likely a transition zone comprised of both accreted material and stars scattered outwards from the inner bulge (Zolotov et al. 2009). There is some tantalizing observational evidence for this two-phase/two-component structure in nearby ETGs (Arnold et al. 2011, Coccato et al. 2010, Forbes et al. 2011; see chapter 3,).

The dynamical signatures of such an assembly history may be discernible in the kinematic structure of nearby ETG stellar halos. However, this approach requires detailed 2D spectroscopy at large galactocentric radius, beyond the typical $\sim 1\, R_e$ spatial scale of current surveys. Our ongoing survey SMEAGOL (Spectroscopic Mapping of Early-type Galaxies to their Outer Limits) aims to extend detailed spectroscopy to $\sim 3\, R_e$ for 25 ETGs (see chapter 2).

Another way to distinguish between the merger and inside-out scenarios is to search for their signatures in the properties of globular cluster (GC) systems of ETGs. Born in major star-forming episodes and passively evolving for many Gyr, GCs are bright, easily identifiable tracers of early galaxy growth and ongoing accretion (e.g., Forbes & Bridges 2010, Mackey et al. 2010). Using GCs to understand the mass assembly histories of a representative sample of nearby ETGs is the key science goal of our other ongoing project SLUGGS (SAGES Legacy Unifying Globulars and Galaxies Survey).

Chapter 2

Wide-Field Stellar Kinematics in Early-Type Galaxies

2.1 Introduction

Recent landmark stellar kinematic studies of galaxies using integral-field unit spectroscopy (Emsellem et al. 2004, Cappellari et al. 2011) have rapidly advanced our understanding of the structure of ETGs. Prior to these surveys, ETGs were typically subdivided into boxy and disky varieties (Kormendy & Bender 1996) based on the deviation in the shapes of their isophotes from pure ellipses. While this division does encapsulate a real physical distinction between pure spheroids and ellipticals with embedded disks, it is also inclination dependent, and thus imperfect as a classification metric. With 2D spatially resolved absorption line stellar kinematics measured for 48 galaxies out to a radius of nearly $1\,R_e$, the SAURON survey team were able to define a more physically motivated division based on projected stellar angular momentum within $1\,R_e$ (λ_{R_e}, Emsellem et al. 2007). This metric, which subdivides ETGs into fast and slow rotator sub-types, was later revised to also incorporate flattening (Emsellem et al.

2011). Importantly, this criteria does not depend on inclination or morphology, thus erasing most of the distinction between disky ellipticals and S0s which are otherwise quite similar in terms of kinematic structure within $1\,R_e$.

Fast rotators (FRs) have more net projected angular momentum and thus larger λ_{R_e} values. They are diskier, more likely to have power-law central surface brightness profiles, exhibit regular aligned rotation, and are generally consistent with oblate axisymmetry with moderate radial anisotropy (e.g., Cappellari et al. 2007). Slow rotators (SRs) on the other hand have little net angular momentum (within $1\,R_e$), are rounder, boxier, typically more massive, have cored surface brightness profiles, and exhibit complex structures such as kinematic twisting, misalignment, and kinematically distinct or decoupled cores.

However, a key limitation of essentially all previous kinematic studies of ETGs is their limited field-of-view. While the inner effective radius encloses half the light of the galaxy by definition, it encapsulates just a tiny fraction of the total mass and angular momentum. Furthermore, inside-out formation scenarios for the mass-assembly of ETGs (e.g., Bezanson et al. 2009) suggest that these galaxies have two distinct zones – an inner component primarily composed of stars formed in-situ at $z \approx 2-3$, and an outer accreted component formed from the stripped stars of many minor-merging partners (Naab et al. 2009, Oser et al. 2010; 2011). Consequently, kinematic surveys targeting the inner few kpc of nearby ETGs (e.g., ATLAS^{3D}; Cappellari et al. 2011) likely contain valuable information about the formation of ancient in-situ bulges. However, a more complete view of the mass assembly of present day ETGs including the formation of extended stellar halos requires a larger perspective that extends to multiple R_e.

Long-slit measurements sometimes extend to larger radius, but are typically only available along the major and minor axes of a galaxy, and thus do not capture enough spatial information (but see Statler & Smecker-Hane 1999). Recently, deep spectra have been obtained for several galaxies out to $3-4\,R_e$ using multiple pointings of the VIRUS-P Integral field spec-

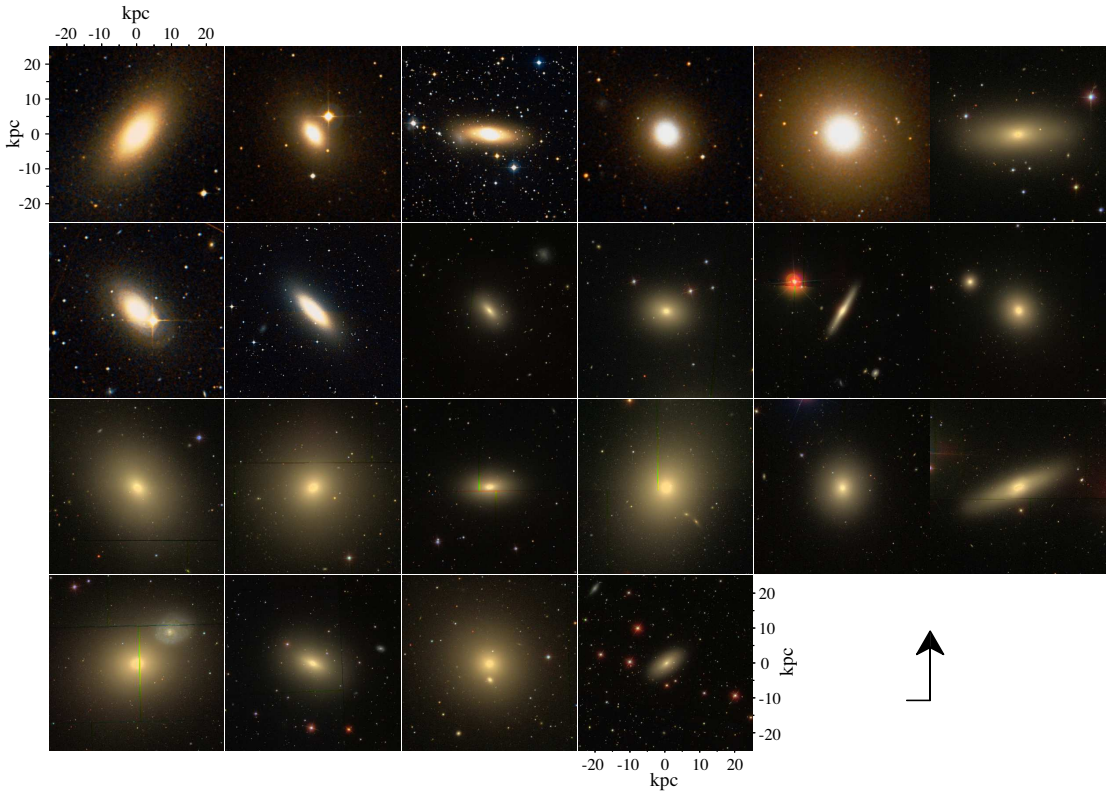

Figure 2.1: Color images of each galaxy, displayed on the same physical scale. Images were taken from the Sloan Digital Sky Survey (SDSS) where available, and the Digital Sky Survey (DSS) otherwise using sky-map.org. Galaxies are ordered left to right, top to bottom by ascending NGC number. **Row 1**: NGC 720, 821, 1023, 1400, 1407, 2768. **Row 2**: NGC 2974, 3115, 3377, 3608, 4111, 4278. **Row 3**: NGC 4365, 4374, 4473, 4486, 4494, 4526. **Row 4**: NGC 4649, 4697, 5846, 7457.

trograph (NGC 4486; Murphy et al. 2011) and the SAURON Integral field unit (NGC 821, NGC 3379; Weijmans et al. 2009); though both of these studies also suffer from sparse spatial coverage.

The technique adopted here produces spatially-well-sampled 2D spectra to $\sim$3 R_e using multi-slit masks and the Keck/DEIMOS spectrograph to obtain stellar kinematics from multiple slits (SKiMS; Norris et al. 2008, Proctor et al. 2009). Pioneering applications of this method for 6 galaxies (NGC 821, NGC 1400, NGC 1407, NGC 2768, NGC 3115, and NGC 4494) have been previously reported (Proctor et al. 2009, Foster et al. 2011, Arnold et al. 2011). Here, we

present wide-field stellar kinematic maps for a total of 22 galaxies; including a reanalysis of the above mentioned systems using new observations and an updated sky-subtraction methodology.

These galaxies were observed as part of the ongoing SLUGGS survey[1] of early-type galaxies in the local universe ($D < 30$ Mpc). A key goal of our survey is to target a representative sample of early-type galaxies, spanning a range of luminosities, morphologies, and environments. The diversity in shape and intrinsic brightness of our sample is immediately obvious from Figure 3.1, which displays color images of each galaxy on a common spatial scale. In terms of environment, five are field galaxies (23%), eleven are in groups (50%), and six are in clusters (27%).

We describe the observational methodology and data reduction process in section 2.2. In section 2.3, we describe our kinematic measurements of V, σ, h_3, and h_4, and perform repeatability tests and literature comparisons. A novel 2D smoothing algorithm, described in section 2.4, is used to produce wide-field two-dimensional kinematic maps for our sample of local universe ETGs (section 2.5). We briefly explore some general kinematic trends of the sample in section 2.6 before concluding (section 2.7).

2.2 Data

The SLUGGS observational strategy is designed around obtaining precise radial velocities of individual globular clusters around nearby ETGs (Brodie et al., in prep). This is accomplished using custom made multi-slit masks and the DEep Imaging Multi-Object Spectrograph (DEIMOS; Faber 2003) at the Nasmyth focus of the 10-meter Keck II telescope. DEIMOS is a wide field ($16.7' \times 5'$) highly-multiplexing ($>$ 100 slitlets per slitmask) spectrograph equipped with a flexure compensation system, making it well suited for precision kinematic studies. We

[1] http://sluggs.ucolick.org

Table 2.1: Properties of suveyed galaxies I

Galaxy NGC (1)	R.A. h m s (2)	Dec. d m s (3)	R_e (arcsec) (4)	λ_{R_e} (5)	Rot_{R_e} (6)	M_K (mag) (7)
0720	01 53 00.5	−13 44 19	33.9	0.12	F	-24.9
0821	02 08 21.1	+10 59 42	39.8	0.27	F	-24.0
1023	02 40 24.0	+39 03 48	47.9	0.39	F	-24.0
1400	03 39 30.8	−18 41 17	29.3	—	F	-24.3
1407	03 40 11.8	−18 34 48	63.4	—	S	-25.6
2768	09 11 37.5	+60 02 14	63.1	0.25	F	-24.7
2974	09 42 33.3	−03 41 57	39.0	0.66	F	-23.6
3115	10 05 14.0	−07 43 07	32.1	—	F	-24.0
3377	10 47 42.3	+13 59 09	35.5	0.52	F	-22.8
3608	11 16 58.9	+18 08 55	29.5	0.04	S	-23.7
4111	12 07 03.1	+43 03 57	12.0	0.62	F	-23.3
4278	12 20 06.8	+29 16 51	31.6	0.18	F	-23.8
4365	12 24 28.3	+07 19 04	52.5	0.09	S	-25.2
4374	12 25 03.7	+12 53 13	52.5	0.02	S	-25.1
4473	12 29 48.9	+13 25 46	26.9	0.23	F	-23.8
4486	12 30 49.4	+12 23 28	81.3	0.02	S	-25.4
4494	12 31 24.1	+25 46 31	49.0	0.21	F	-24.1
4526	12 34 03.1	+07 41 58	44.7	0.45	F	-24.6
4649	12 43 40.0	+11 33 10	66.1	0.13	F	-25.5
4697	12 48 35.9	−05 48 03	61.7	0.32	F	-23.9
5846	15 06 29.3	+01 36 20	58.9	0.03	S	-25.0
7457	23 00 59.9	+30 08 42	36.3	0.52	F	-22.4

Notes: (1) Galaxy NGC number. (2) Right ascension and (3) declination (J2000) taken from the NASA/IPAC Extragalactic database (NED). (4) Circularized effective (half-light) radius in units of arcseconds. Effective radii for ATLAS^{3D}galaxies are taken from Cappellari et al. (2011), the remaining values (for NGC 720, NGC 1400, NGC 1407, NGC 3115) were derived using the same methodology. (5) Dimensionless proxy for stellar specific angular momentum within 1 R_e (see Emsellem et al. 2007) with the majority of values from Emsellem et al. (2011). The λ_{R_e} value for NGC 720 is from Cappellari et al. (2007). No values are reported for galaxies without available IFU data. (6) Central fast (F) or slow (S) rotator designation; values from Emsellem et al. (2011) and Cappellari et al. (2007), or derived from available kinematic data (for NGC 1400, NGC 1407, NGC 3115) using the original criteria from Emsellem et al. (2007). (7) Extinction corrected absolute K-band magnitudes derived from the 2MASS extended source catalog (Jarrett et al. 2000). Values taken from Emsellem et al. (2011) or measured using the same methodology for galaxies not in the the ATLAS^{3D}sample.

Table 2.2: Properties of suveyed galaxies II

Galaxy NGC	Morph	PA (deg)	ϵ	V_{sys} (km s^{-1})	Dist (Mpc)	Env.
(1)	(8)	(9)	(10)	(11)	(12)	(13)
0720	E5	142.3	0.43	1745	26.9	F
0821	E6	31.2	0.35	1718	23.4	F
1023	SB0	83.3	0.36	602	11.1	G
1400	E-S0	36.1	0.11	558	25.7	G
1407	E0	58.3	0.05	1779	28.1	G
2768	S0	91.6	0.47	1353	21.8	G
2974	E4	44.2	0.41	1887	20.9	F
3115	S0	43.5	0.49	700	9.4	F
3377	E5-6	46.3	0.50	690	10.9	G
3608	E5-6	82.0	0.19	1226	22.3	G
4111	E1-2	150.3	0.58	792	14.6	G
4278	E1-2	39.5	0.10	620	15.6	G
4365	E3	40.9	0.25	1243	23.3	G
4374	E3	128.8	0.15	1017	18.5	C
4473	E5-6	92.2	0.42	2260	15.3	C
4486	E0-1	151.3	0.04	1284	17.7	C
4494	E1-2	176.3	0.17	1342	16.6	G
4526	SAB0	113.7	0.36	617	16.4	C
4649	E2	91.3	0.16	1110	17.3	C
4697	E2	67.2	0.45	1252	11.4	G
5846	E0-1	53.3	0.06	1712	24.2	G
7457	S0	124.8	0.47	844	12.9	F

Notes: (1) Galaxy NGC number. (2) Morphology. (3) Photometric position angles and (4) ellipticities. Values for ATLAS^{3D}galaxies are from Krajnović et al. (2011), NGC 720 from Cappellari et al. (2007), NGC 1400 and NGC 1407 from Spolaor et al. (2008), and NGC 3115 from Capaccioli et al. (1987). (5) Systemic velocity in km s^{-1}. (6) Distances measured in Mpc from Tonry et al. (2001) using the -0.06 mag offset suggested in Blakeslee et al. (2010). (7) Local environment type: field (F), group (G), or cluster (C).

make optimal use of this instrument by extracting integrated galaxy-stellar-light spectra from the background regions of slits placed on globular clusters, thereby obtaining both types of spectra simultaneously. The kinematic measurements measured from these stellar spectra (SKiMS; Stellar Kinematics from Multiple Slits) are presented in section 2.5, while the globular cluster measurements are presented in Pota et al. (2013) and references therein.

2.2.1 Observations

DEIMOS has a roughly rectangular field-of-view with a few missing regions (see top of Figure 2.2). For comparison, the average galaxy effective radius in our sample is less than an arcminute. A single slitmask contains ∼100 slits, each with a minimum length of 4 arcseconds. Additional filler slits are sometimes placed near the galaxy when there are no suitable globular cluster candidates, and also at large radius to get sky spectra that are virtually uncontaminated by galaxy light. Normally, at least 4 slitmasks are observed per galaxy, and are arranged in a spoke pattern centered on the galaxy to ensure good azimuthal coverage (see Figure 2.2 for an example).

We collected $\sim 10,000$ spectra for 22 galaxies over the course of 7 years and 19 observing runs. Our baseline observing recipe is to integrate on a mask for 2 hours in a series of 4 exposures, though conditions frequently cause deviations from this plan. The resulting spectra are quite deep and permit kinematic information to be extracted from individual slits at surface brightnesses fainter than $\mu_i = 23\,\mathrm{mag\,arcsec^{-2}}$ (see Figure 2.3).

All of the spectra discussed here were obtained using a 1200 line mm^{-1} grating centered at 7800 Å, and a 5500 Å order-blocking filter. This setup is optimized to target the near-infrared (NIR) Calcium II triplet, with prominent lines at 8498, 8542, and 8662 Å. In this wavelength range the typical spectral dispersion of $0.32\,\text{Å}\,\mathrm{pixel}^{-1}$ translates to a velocity scale of $11\,\mathrm{km\,s^{-1}\,pixel^{-1}}$. With a slit width of 1 arcsecond, the average FWHM resolution is 1.6 Å,

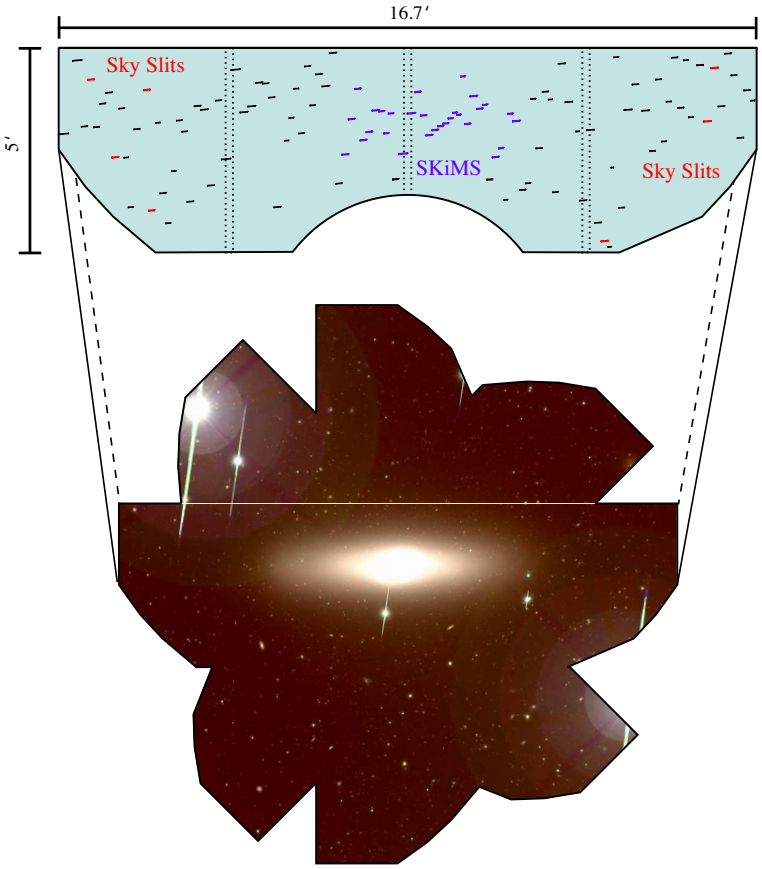

Figure 2.2: Observational footprint of multi-slit DEIMOS observations. The shape of a 16.7' x 5' DEIMOS slitmask is shown at top. Short lines denote milled slits, with selected sky slits shown in red, and selected SKiMS slits in purple. Vertical dotted lines denote chip gaps. Bottom: A gri composite Subaru/Suprime-Cam image of NGC 4526 with the areal coverage of 4 slitmasks arranged in a spoke pattern.

or equivalently $\sim$56 km/s (see also Figure 2.4).

2.2.2 Data Reduction and Sky Subtraction

The DEIMOS spectra were all reduced using a modified version of the `spec2D` pipeline (Cooper et al. 2012). The pipeline uses internal quartz-lamp flatfields to rectify each slit, measure a slit function, and make a fringing correction. Wavelength solutions are computed from NeArXeNe arclamp spectra taken through each mask. The background spectrum in each slit is modeled

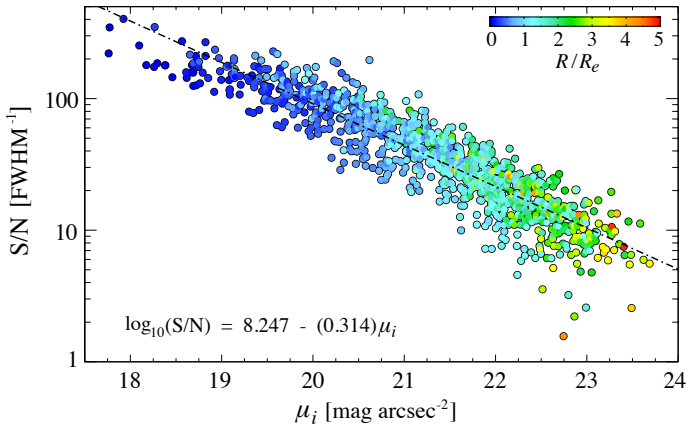

Figure 2.3: Photometric depth of the DEIMOS measurements. Spectral S/N plotted versus the local i-band surface brightness around each measurement location. Surface brightness values are measured from SDSS images, and only spectra from those galaxies within the SDSS footprint are shown. Points are colored according to galactocentric radius normalized by R_e (see color bar at top-right). There is a roughly linear relation, shown at bottom-left, between the base-10 logarithm of the spectral S/N and the local surface brightness.

as a b-spline and the separate exposures are co-added together before a final one-dimensional spectrum is produced. We modified the pipeline to additionally return the associated pixel-by-pixel inverse variance array for use during kinematic fitting.

Each background spectrum extracted from a slit is composed of two primary components: the integrated galaxy light that we are ultimately interested in, and foreground sky that must be subtracted out. An accurate measure of the latter component is crucial given the strong and variable emission of the night sky in the NIR. Fortunately, the large field-of-view of DEIMOS relative to the luminous size of the galaxies under study means that there are numerous sky-slits towards the edges of each mask that are essentially free of galaxy light. We select a number of these slits in order to build up a suitable catalog of sky spectra for each mask. Specific care is taken to avoid slits with vignetting or other reduction issues that become more common towards the edges. Also, for reasons that are explained below, we select sky spectra from a variety of positions across the short axis of the mask.

The next step would usually involve constructing a single high-S/N master sky spectrum by co-adding several of the selected sky-spectra (see e.g., Proctor et al. 2009, Foster et al. 2011). However, application of the conventional approach was complicated by the discovery of a spatially dependent resolution in DEIMOS. Slits located at the bottom of a slitmask have slightly higher resolution (smaller FWHM) than slits placed near the top (see Figure 2.4). Consequently, the spectrum from an arbitrarily placed slit will often have a different resolution than the constructed master sky spectrum.

Ultimately, the effect is subtle, with the FWHM changing by less than a pixel between the top and bottom of the mask. However, we wanted to make every attempt at optimizing the sky subtraction given the potential for large residuals from strong near-infrared sky lines. We opted to use `pPXF` (Penalized Pixel-Fitting method; Cappellari & Emsellem 2004) to construct a unique sky spectrum for each slit, modeled as a weighted combination of the input sky spectra. This approach is suitable for sky-dominated spectra, which is the case for the vast majority of our data, and should result in a very accurate sky subtraction (see e.g., Weijmans et al. 2009). An example of a sky-subtracted science spectrum can be see in the left-hand panel of Figure 2.5. (middle-line).

2.3 Kinematic Measurements

The LOSVD (line-of-sight velocity distribution) of each spectrum is parameterized as a truncated Gauss-Hermite series (van der Marel & Franx 1993, Gerhard 1993); including V (mean velocity), σ (velocity dispersion), h_3 (a measure of skewness), and h_4 (a measure of kurtosis). These parameters are measured in pixel space using the `pPXF` software. The best fitting solution is determined by finding the weighted combination of template stars, that when convolved by the parameterized LOSVD, most closely matches the input spectrum in a maximum

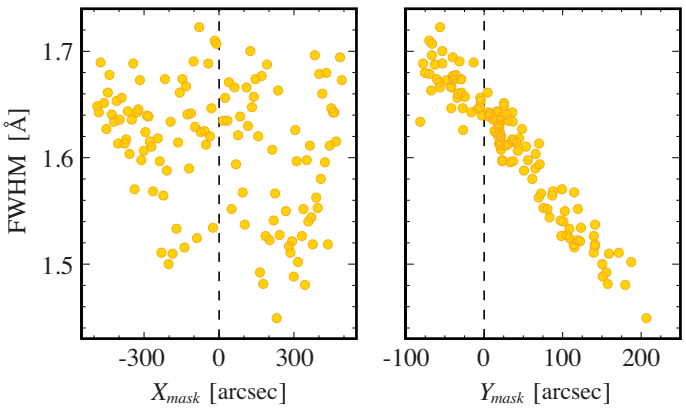

Figure 2.4: Spatial dependence in DEIMOS spectral resolution. Measured resolution as a function of x-position (long-axis; left) and y-position (right) across a single DEIMOS slit mask. FWHM values are measured from a night sky emission line (at 8415 Å) in the background spectrum of each slit. The resolution appears uncorrelated with x-position on the mask, but has a clear dependence on y-position.

likelihood sense. We include a 4^{th} order additive legendre polynomial to account for deviations in continuum shape between our spectra and the template stars.

A potential pitfall in making kinematic measurements on low S/N spectra is fitting noise in the spectrum with anomalous h_3 and h_4 values. To help guard against this, `pPXF` uses regularization in the form of a penalty term that biases the fit towards a Gaussian when the S/N of a spectrum is insufficient to constrain the higher order moments of the LOSVD. From the Bayesian perspective, this is equivalent to imposing a prior on the h_3 and h_4 parameters that encapulates the notion that higher order moments are less likely to be constrained as S/N decreases. A non-zero penalty requires a minimum decrease in the variance of the fit residuals in order to accept a larger amplitude h_3 or h_4 value (see Cappellari & Emsellem 2004). While this penalization results in a bias towards Gaussian LOSVDs, it also reduces the likelihood of measuring spurious higher order moments.

The appropriate penalty value is at the very least resolution and S/N dependent, and

can be determined via Monte-Carlo simulation. Following the method outlined in Cappellari et al. (2011), we measured the requisite penalty at a range of S/N levels, and fitted these results with a 3rd order polynomial. The coefficients are $c_0 = 0.119$, $c_1 = 5.76\times10^{-3}$, $c_2 = -1.26\times10^{-5}$, and $c_3 = 9.37 \times 10^{-9}$. The penalty value for a given science spectrum is determined using its measured S/N and the above polynomial.

We restrict the `pPXF` fit to the spectral region immediately surrounding the NIR Calcium II triplet between 8480 Å and 8750 Å. The latter bound was increased on a galaxy-by-galaxy basis when a high systemic velocity redshifted the wings of the reddest CaT feature anywhere near the wavelength cutoff (e.g., NGC 4473). No skylines are explicitly masked out since those pixels should, in principle, be appropriately weighted by the inverse variance arrays. However, we do allow for outlying pixel values to be clipped, which can occur when skylines are improperly subtracted.

Template mismatch can be an issue with this method, so an appropriate suite of input template stars is usually crucial. Fortunately, the NIR CaT is fairly insensitive to these issues (Barth et al. 2002). Previous SKiMS analyses (e.g., Proctor et al. 2009) used 13 template stars observed with DEIMOS that included both giant and main sequence stars at several different metallicities. Here, we use an expanded set of 42 stars carefully selected from the Cenarro et al. (2001) library of 706 stars. The primary differences in the new template catalog are the inclusion of main sequence early-type stars to allow for the presence of Paschen lines, and M-type dwarfs to account for any molecular absorption features. The resolution of the selected template stars is 1.5 Å, which is well matched to the spectral resolution of our spectra (1.5 – 1.7 Å).

`pPXF` requires reasonable initial guesses of the V and σ fitting parameters in order to efficiently find the best fitting LOSVDs. This is especially important for lower S/N spectra where noise artifacts (e.g., large skyline residuals) can create likelihood barriers in parameter space. Thus, we devised the following automated method for finding reasonable initial parameter

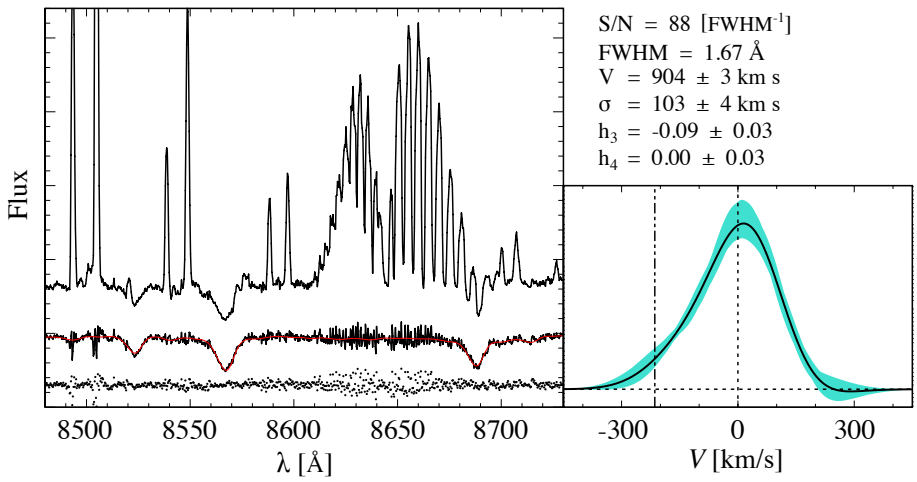

Figure 2.5: LOSVD extraction. Left: A fiducial raw spectrum with galaxy stellar light and night-sky background (top); sky subtracted spectrum with best fit model overlaid in red (middle); and fitting residuals (bottom). Right: Best fitting parameterized LOSVD (solid black line). The envelope (solid cyan) shows the range of possible solutions as determined from 100 Monte-Carlo realizations of the best fit model with added noise. The vertical dot-dashed line marks the systemic velocity of the galaxy.

values. First, we create a grid of 120 (V,σ) pairs that span a realistic range of values for the galaxies under study. Second, we run `pPXF` in two moment mode (i.e., not fitting h_3 or h_4) using each of these pairs as initial guesses. Third, the resulting ensemble of solutions and reduced chi-squared values are used to determine the best initial guesses of V and σ. Finally, these values and the appropriate penalty terms are used to run `pPXF` in four moment mode to derive the V, σ, h_3, and h_4 values that maximize the likelihood function.

After determining the best fitting LOSVD for each spectrum, a Monte-Carlo method is used to estimate the uncertainty of each kinematic parameter (V, σ, h_3, h_4). First, we use the best-fit model LOSVD to create a realization of each spectrum, and then add noise using the inverse variance array. Each model spectrum is subsequently refitted using `pPXF` with the penalty set to 0 to derive conservative error estimates as suggested by Cappellari & Emsellem (2004). This process is repeated 100 times per spectrum, with the error on each kinematic

parameter taken as the standard deviation of the returned values. The best fitting solutions generally have $\tilde{\chi}^2 \leq 1$, indicating that the inverse variance arrays are realistic estimators of the pixel-by-pixel uncertainties of the spectra. In those cases where $\tilde{\chi}^2 > 1$, we attempted to derive conservative Monte-Carlo errors by multiplicatively scaling the inverse variance array such that $\tilde{\chi}^2 = 1$. Finally, the measured velocities are corrected for heliocentric motion, and each individual fitted spectrum is inspected by eye for quality control. The right panel of Figure 2.5 shows an example of a reconstructed LOSVD and its 99% uncertainty envelope.

2.3.1 Measurement Repeatability

Repeated spectroscopic measurements can be useful in assessing the accuracy of Monte-Carlo error estimates and in identifying unaccounted-for systematic error terms. We define two spectra to be co-spatial (i.e. repeated) if they are within 3 arcseconds of each other. This search radius is small enough to ensure that only spectra from separate masks are paired. Figure 2.6 shows the difference between repeat measurements, normalized by their Monte-Carlo errors added in quadrature, versus the average S/N per resolution element of each spectrum. If the Monte-Carlo errors capture all sources of uncertainty in the measurements, then the standard deviation of normalized differences should be nearly unity (i.e. $\tilde{\chi}^2 = 1$). Indeed, this is case for the vast majority of the measurements, reflecting the superb measurement precision and stability of the DEIMOS spectrograph.

However, it is also clear that the distribution widens with increasing S/N, indicating underestimated uncertainties for the brightest spectra. This behavior is expected when there are small systematic error terms that only become non-negligible when the Monte-Carlo error approaches zero. After some experimentation, we measured systematic errors in V and σ of 5 $\mathrm{km\,s^{-1}}$ and 6 $\mathrm{km\,s^{-1}}$, respectively. These values are added in quadrature to the previously derived Monte-Carlo error estimates. The uncertainties on h_3 and h_4 were already conservative,

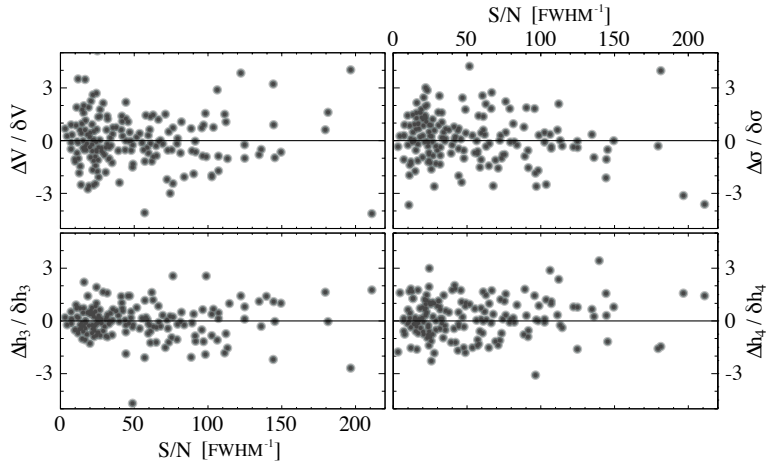

Figure 2.6: Repeatability of measured velocity moments. The difference (Δ) between measurements from spectra that are co-spatial to within 3 arcseconds versus S/N per resolution element. Each Δ value is normalized by the measurement errors added in quadrature. If the derived errors, for mean velocity (top-left), velocity dispersion (top-right), h_3 (bottom-left), and h_4 (bottom-right), fully accounted for the true measurement error, then the standard deviation of the values on the y-axis would be exactly 1 in each panel. However, at high S/N, both velocity and velocity dispersion show anomalously high values, suggestive of underestimated errors or a small systematic error term (see text).

leading to no apparent need for additional systematic error terms.

2.3.2 Literature Comparisons

While the majority of the DEIMOS spectra are at radii beyond $1\,R_e$, there are still a fair number of spectra that are within the SAURON observational footprint. The galaxies in common between the two surveys span a range of systemic velocities, velocity dispersions, h_3, and h_4 values, providing a valuable opportunity to carefully cross check measured kinematic quantities. Figure 2.7 shows a comparison between measurements from each survey that are spatially coincident to within 3 arcseconds. The solid black lines in each panel are linear fits to the measurements that take x and y-axis error bars into account while the dot-dashed lines show the 1:1 relation.

A few things are immediately obvious from this figure. For instance, the general agree-

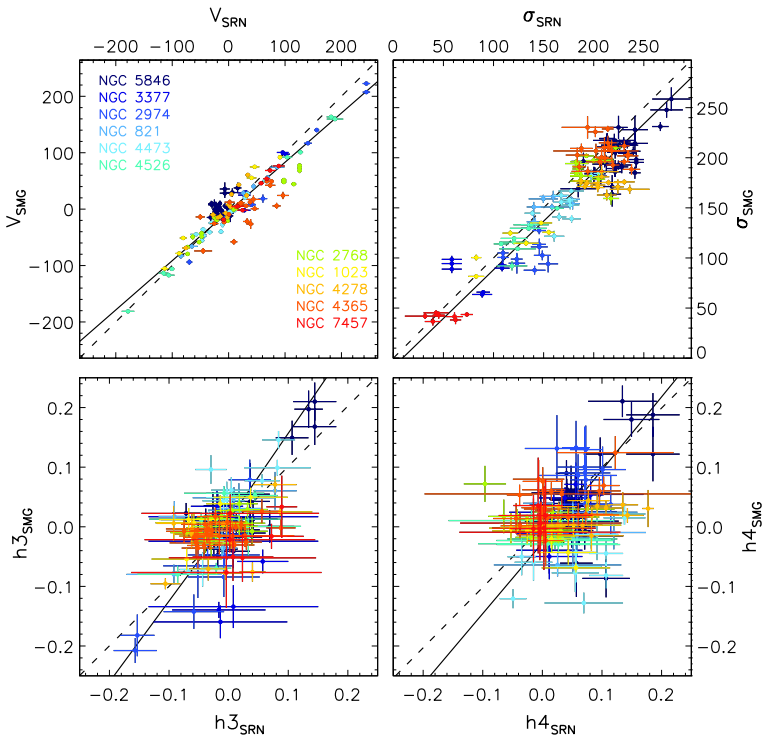

Figure 2.7: Literature comparison of kinematic measurements. Comparison between our measured values (y axes) and literature values from the SAURON survey (x axes). Mean velocity (top-left), velocity dispersion (top-right), h_3 (bottom-left), and h_4 (bottom-right). Points are color coded according to galaxy, as shown in the key in the top-left panel. The dot-dashed line is a 1:1 relation, while the solid black line denotes the best fitting linear relation to the data.

ment between the two surveys is generally very good, with the measurements showing a high degree of correlation. However, it is also clear that the SAURON velocity dispersions are systematically higher than DEIMOS dispersions by 15 $\mathrm{km\,s^{-1}}$ (see Fig. 5, Proctor et al. 2009, cf.; Murphy et al. 2011). There is also a tendency for the SAURON h_3 and h_4 amplitudes to be larger than the corresponding DEIMOS values.

Before discussing some specific galaxies, we should point out some important caveats regarding this comparison. First of all, most of the matched spectra are near the outer edge of the SAURON field-of-view, and therefore represent some of the noisier and more aggressively co-added measurements from that survey. Conversely, these data comprise the high S/N tail of

our DEIMOS observations. Second, the spectral resolution and dispersions of each instrument are quite different. Operating in low resolution mode, SAURON has an instrumental velocity resolution of $\sigma_{inst} = 108$ km s^{-1} and a dispersion of 66 km s^{-1} pixel^{-1}. The corresponding values for our DEIMOS measurements are 24 km s^{-1} and 11 km s^{-1} pixel^{-1}. Third, and perhaps most importantly, these two surveys utilize very different spectral regions, with SAURON probing shorter wavelengths (4800 – 5380 Å) than DEIMOS (8480 – 8750 Å). There are both benefits and drawbacks to working with spectra within each of these wavelength ranges. LOSVD fitting at bluer wavelengths benefits from more absorption features and fewer skylines than in the NIR. However, this range is also more complicated, can have emission lines to contend with, and is sensitive to template mismatch issues that do not effect the NIR CaT (Barth et al. 2002).

Despite the general accordance in derived values between the two surveys there are some noticeable systematic differences. For example, in NGC 7457 the matched SAURON velocity dispersion values range between 30 and 70 km s^{-1}, while the corresponding DEIMOS values cluster tightly around 40 km s^{-1}. It seems plausible that this discrepancy is caused by sampling issues in the SAURON spectra since these velocity dispersions are at or below the spectral dispersion. However, a similar discrepancy in NGC 4278 is harder to account for given that the velocity dispersions involved are easily resolved by both spectrographs. For this galaxy, the SAURON velocity dispersions range between 180 and 240 km s^{-1}, while the corresponding DEIMOS values span a much narrower range and top out at 180 km s^{-1}.

Assuming that the disagreement was indicative of some error in our measurements, we performed an extensive set of tests to try and identify the cause. Certain modifications to our fitting recipe, such as altering the catalog of stellar templates, modifying the spectral range, or reducing the order of the additive Legendre polynomial, could have small systematic effects on the results but were ultimately unable to erase the discrepancy. We also explored whether this issue could be caused by the systemic velocity of NGC 4278 redshifting the calcium triplet

feature into a particularly unfortunate wavelength range with respect to the strong NIR sky lines. However, a number of Monte-Carlo tests with simulated input spectra revealed no evidence for such an effect. Ultimately, we were unable to account for the discrepancy – leaving open the possibility that the offset is due to either some unknown systematic error or is indicative of something physical. We note that NGC 4278 is one of the galaxies in the SAURON sample that is listed as an emission line galaxy, a point that could be relevant in either case.

2.3.3 Stellar Populations and Wavelength

The conventional wisdom is that ETGs are primarily composed of old stars. However, accretion can bring in small amounts of gas that reinvigorate star formation for short periods of time, thus contaminating the predominantly old stellar population with some number of young stars. Given a dissipational origin, this young stellar component may then exhibit its own distinct kinematic structure; e.g., it could be both colder and more rapidly rotating than the preexisting stars. Since young stellar populations emit more of their light in the blue region of the spectrum, we were interested to know whether adding a young stellar component led to measured LOSVD shapes that were systematically different between blue and red spectral regions. Specifically, will a small population of young stars yield different kinematic measurements at blue wavelengths ($4800 - 5380\,\text{Å}$) than at red wavelengths ($8480 - 8750\,\text{Å}$)?

To test for this differential sensitivity to young stars, we created a set of composite spectra using the MILES single stellar population (SSP) model spectra (Vazdekis et al. 2010). Each composite spectrum contains a particular mass fraction of younger (3 Gyr) stars ranging between 0 and 100%, with the balance made up of old (10 Gyr) stars. To keep the test simple, we kept both sub-populations at solar metallicity. To simulate the effect of a moderately rotating component, we convolved the 3 Gyr old SSP spectrum with a Gaussian LOSVD with $V = 100\,km\,s^{-1}$ and $\sigma = 75\,km\,s^{-1}$. Conversely, the 10 Gyr population is meant to represent

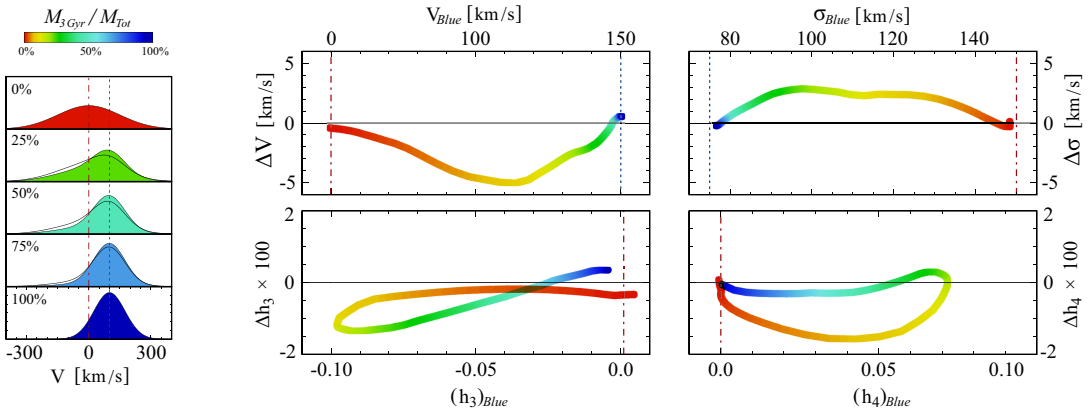

Figure 2.8: Differential kinematic effects of a young stellar component on blue and red spectral regions. Composite SSP spectra are created by combining spectra together from a 3 Gyr and a 10 Gyr old population. The input spectra are first convolved with Gaussian LOSVDs (3 Gyr: $V = 100\,km\,s^{-1}$ and $\sigma = 75\,km\,s^{-1}$) and (10 Gyr: $V = 0\,km\,s^{-1}$ and $\sigma = 150\,km\,s^{-1}$). Fiducial composite LOSVDs are shown at left and colored according to young star fraction. Each panel (at right) shows the difference between the measured LOSVD parameters for red spectra centered on the near-infrared calcium-triplet (8480-8750 $\AA$), and blue spectra ($4800 - 5380$ Å). If both spectral regions were equally sensitive to young stars, the curves would all be horizontal indicating exactly equal measurements. While there is some obvious differential sensitivity apparent, the amplitude of the difference is small enough to be ignored given the typical uncertainties on these parameters for our spectra.

a dynamically hotter and slowly rotating spheroid, and was thus convolved with a Gaussian LOSVD with $V = 0\,km\,s^{-1}$ and $\sigma = 150\,km\,s^{-1}$.

If the young stellar population preferentially affects the blue spectral measurements, then we should detect a systematic offset in the derived kinematic parameters between the red and blue spectra. Specifically, we expect that the LOSVD parameters derived from the blue spectra will be biased towards the kinematics of the young stellar population. We used `pPXF` to measure the kinematic parameters for each composite spectrum separately in the blue and red wavelength ranges. The results are shown in Figure 2.8. Filled curves (at left) show the LOSVDs for composite spectra with a young star fraction of 0, 25, 50, 75, and 100%. We note that young stellar populations are brighter than older populations, which results in a natural overrepresentation of younger stars in the LOSVD. The overlaid black curves show the

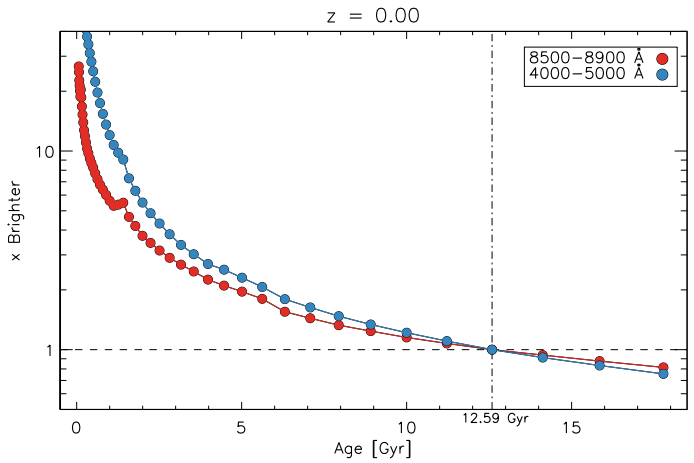

Figure 2.9: Stellar population continuum brightness with age. The continuum brightness of SSPs decrease with age, but not equally at all wavelengths. We plot the continuum luminosity of a solar metallicity SSP as a function of age, normalized by the luminosity at 12.59 Gyr. We include separate curves for the continuum between 4000-5000 Å (blue-line), and 8500-8900 Å (red-line). Ultimately, the decrease in continuum brightness with age is similar for these two wavelength intervals, with a tendency for young stars to shine brighter at bluer wavelengths. The implication is that blue spectra are only slightly more sensitive to the contaminating effects of young stars compared to near-infrared spectra.

resulting LOSVDs if this luminosity difference were unaccounted for. Importantly, the relative brightnesses of young and old stellar populations are similar in the chosen blue and red spectral ranges (see Figure 2.9). This means that red and blue spectra are roughly equally effected by young (3 Gyr) stellar populations, and thus no significant differential sensitivity to young stars is expected.

The right panels of Figure 2.8 illustrate this point a bit more clearly. In each panel we plot the difference in the measured kinematic quantity between the red and blue spectral regions versus its value as measured in just the blue spectral region. The curve follows our ensemble of composite spectra from a young-star fraction of 0% to 100% as shown by the colorbar at top-left. When the young star fraction is 0, the spectrum contains only old stars and has a purely Gaussian LOSVD with zero mean velocity and a velocity dispersion of $150\,km\,s^{-1}$. As the

young star fraction increases, the composite LOSVDs becomes non-Gaussian (non-zero h_3 and h_4) until the population is purely made of young stars and the LOSVD is again Gaussian. Note that this effect is very non-linear in that a small amount of young stars is able to appreciably shift all four kinematic parameters; a consequence of the extremely bright intrinsic luminosity of young stellar-populations.

If the red and blue spectra were equally effected by the young stellar population, then each curve would would be exactly horizontal. While this is not strictly the case, the deviations are small enough to be considered negligible given the typical uncertainties of our stellar kinematic measurements. In other words, there is relatively little differential sensitivity to stellar population effects between these wavelength regions. This simple test suggests that the discrepancies in measured kinematic values between the SAURON and SLUGGS datasets (see Section 2.3.2) are not caused by a differential sensitivity to young stellar populations in the different wavelength ranges used in each survey.

2.3.4 Folding-In Literature Measurements

Exploring the causes behind discrepant kinematic measurements across different spectral ranges is an important and potentially interesting topic to pursue. However, the primary focus of this paper is to present the large scale kinematic structure of ETGs, and to highlight general trends with radius. To do this, we will be combining SAURON and other literature datasets with our own in order to construct kinematic maps (see next section). Since we are concerned with general trends, we remove the mean systematic offset between datasets so that the final maps do not have unphysical step functions in them.

2.4 Kinematic Mapping

In this section we outline the methodology used to create two-dimensional maps of V, σ, h_3, and h_4, for each galaxy in our sample. These 2D kinematic maps are meant to provide an immediate sense of large-scale kinematic behavior, and to highlight structures and general trends in the data. While these types of maps are most commonly used to present the data products of IFU observations, they are also well suited for presenting other spatially resolved datasets, such as ours. However, the spatial sampling density resulting from slitmask spectra is quite sparse compared to that of an IFU. This results in large gaps in spatial coverage that require smoothing and/or interpolation to fill.

Previous approaches towards solving this problem include using a kinemetric model (Proctor et al. 2009), and kriging fitting (Arnold et al. 2011). Both of these methods have certain downsides, e.g., the former requires a specific parameterization, while the latter is prone to over-smoothing or ringing. Instead, we use a new methodology that requires no parameterization, preserves much of the spatial information, and modestly smooths the data to suppress noisy measurements.

2.4.1 Smoothing Algorithm

We account for the empty regions between spectra by generating a Voronoi tessellation that assigns a spatial Voronoi bin to each stellar spectrum. For example, the locations of the stellar spectra for NGC 821 are plotted in Figure 2.10(b), with the corresponding Voronoi bins visible as monochromatic polygons in Figure 2.10(c). We point out that the raw velocity map displayed in Figure 2.10(c) is noisy enough to obscure the general kinematic trends in the data, and is not very useful as is. In principle, we could have partially ameliorated this problem by co-adding several noisy spectra together into a single higher S/N spectrum before fitting the

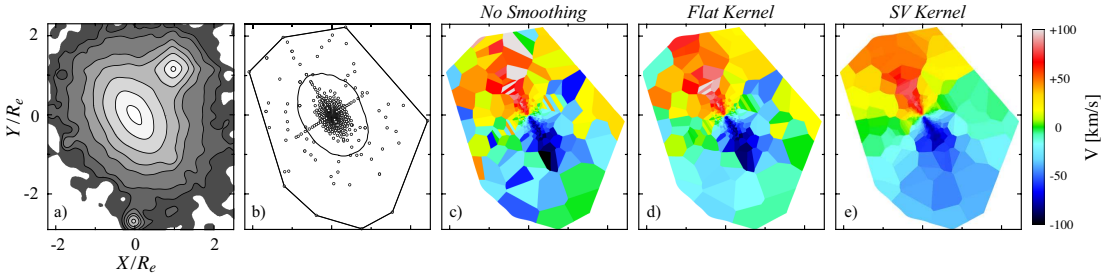

Figure 2.10: Illustration of the interpolation-smoothing method for the velocity data of NGC 821. A contour plot for the I-band DSS image of this galaxy is shown in (a), while the location of each stellar spectrum (SLUGGS + literature) is marked with a black circle in (b). In the latter panel, the inner and outer solid black lines denote the 1 effective radius isophotal contour and the convex hull (i.e., bounding polygon) of the measurement locations, respectively. As a point of comparison, a non-smoothed map of the velocity data is shown in (c). Each solid-colored Voronoi bin corresponds to exactly one velocity measurement, and is colored according to the velocity scale at the far right of the plot. Panels (d) and (e) contain maps that are smoothed using the 2D-moving-window algorithm outlined in section 4.1. The former uses a flat smoothing kernel, corresponding to a straight average, while the latter takes advantage of the spatial correlation information contained in the data by using the empirical semi-variogram as its smoothing kernel.

LOSVD. However, while this approach is suitable for IFU measurements with ample spatial sampling, it would necessarily destroy valuable spatial information in our data. Additionally, many of our large-radius spectra are separated by rather large distances on the sky, and may be unsuitable for direct co-addition since they sample kinematically distinct regions of the galaxy.

A better approach is to smooth the noisy data just enough to bring out the underlying trends, but not so much as to destroy spatial information. A common technique is to use a Gaussian smoothing kernel that de-weights more distant, and thus less correlated points. However, the varying spatial density of measurements makes a single-width Gaussian kernel unsuitable, since it would lead to maps with zones of under or over smoothing. The adaptive Gaussian kernel method used in Coccato et al. (2009) attempts to solve this problem, but still relies on an arbitrarily shaped Gaussian weighting function and an assumed kinematic model for the galaxy.

2.4.1.1 Weighting Function

Here, we use an empirical approach that uses the spatial correlation information contained in each dataset to optimally smooth the associated kinematic maps. For each separate dataset (e.g., h_3 values of NGC 821 or σ values of NGC 1023), we generate a semi-variogram (semi-variance vs. separation, see also Figure 2.11). Semi-variance (γ), as defined in eqn. (2.1), is measured by finding all pairs of values that are separated by a particular distance Δ to within the specified tolerance δ, and then measuring half the variance of their differences:

$$\gamma(\Delta) = \frac{1}{2\,N_S} \sum_{(i,j)\in S}^{N_S} [Z(\vec{x}_i) - Z(\vec{x}_j)]^2 \qquad (2.1)$$
$$S = \{(i,j) : -\delta < \|\vec{x}_i - \vec{x}_j\| - \Delta \leq \delta; i > j\}$$

where $\vec{x}_k$ is the position of the k-th spectrum and $Z(\vec{x}_k)$ is the value of interest at that location.

Figure 2.11 shows the square root of the semi-variance versus separation for the velocity data of NGC 3115. Semi-variance increases with separation because nearly co-spatial values are highly correlated, while distantly separated values are increasingly uncorrelated. For each dataset we fit a polynomial to the semi-variance profile and use its inverted form as an empirical weighting function in the smoothing process outlined below.

2.4.1.2 Grouping Measurements

With the weighting function in hand, the next step is to combine the measurements together to suppress noise while not washing out legitimate large scale structure. Our adopted technique is an extension of the one-dimensional moving-average algorithm, commonly used to filter time-series data, to two dimensions. The basic idea is to estimate the local mean of a

dataset for a series of spatial locations by taking the appropriately weighted average of nearby measurements. A key point here is that individual measurements can belong to many unique groupings of data, each centered at a different spatial location.

The groupings (or clusters) of measurements are selected using a custom two-dimensional search algorithm and the requirement that clusters meet certain connectedness criteria. Each group is assigned a unique identifier, based on the associated measurements, which is added to a hash table to ensure uniqueness. In each cluster, the semi-variance is calculated for each grouped measurement using (i) its distance to the centroid of the cluster and (ii) the polynomial fit for the associated semi-variogram. These values are then combined with the Monte-Carlo error estimates to derive a final weighting factor for each measurement. Next, these weights are used to compute a weighted sum of measurements for each cluster. At this stage, there are many unique clusters which overlap heavily with other groupings. The final step involves combining the overlapping clusters together, associating the results with the Voronoi bins associated with each individual measurement, and creating the final map.

However, we have not yet specified how many points should go into a cluster – a crucial issue since this will control the degree of smoothness in the final map. Importantly, the number of points is not constant, and is determined separately for each grouping of measurements. We require that each cluster contains just enough points such that the resultant error of the weighted sum is within some tolerance (e.g., $\sim 10 - 15$ km s^{-1} for velocity maps). This feature makes the smoothing method naturally adaptive because groupings in high spatial-measurement-density regions will be physically small and localized, and just the opposite in low-density regions. In basic terms, the smoothing is optimized so that the centers of maps are not over-smoothed, and the edges of maps are not under-smoothed.

Figures 2.10(c) and 2.10(e) show maps for the raw and smoothed versions of the NGC 821 velocity data. The latter map reveals far more structure than the former, includ-

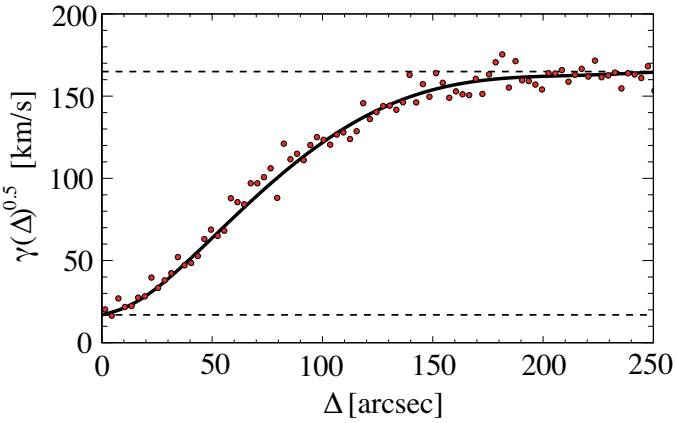

Figure 2.11: Velocity semi-variogram for NGC 3115. The empirical semi-variance $\gamma(\Delta)$ is a measure of how correlated values are as a function of their separation Δ. Points represent the semi-variance measured in discrete bins of separation distance, while the solid line is a polynomial fit to the data. At small separations, the line-of-sight velocities are similar, and the semi-variance is correspondingly small, while at large separations, velocities become essentially uncorrelated. For each velocity moment and galaxy, we use this empirical measure of spatial correlation to determine the appropriate smoothing kernel for the data (as in Figure 2.10).

ing a falling rotational amplitude along the major-axis. For comparison, 2.10(d) shows the map that results from a flat weighting kernel, which is similar to taking a straight average in each cluster.

2.5 Two-Dimensional Kinematic Maps

Wide-field absorption-line stellar kinematic maps for the 22 ETGs in our sample are displayed in Figure 2.12. Each map of V, σ, h_3, and h_4 is optimally smoothed (see previous section) to highlight large scale trends in the kinematics while preserving the detailed structure evident at the centers of those galaxies from IFU measurements. Despite some residual noise, it is clear that these galaxies exhibit a wide variety of kinematic structures on these large spatial scales and generally have LOSVDs that are non-Gaussian at the few percent level.

In Figure 2.12 the data for each galaxy are laid out as follows. At left, the galaxy's

name is listed above the isophotal contour map of the respective I-band DSS image – oriented so that the photometric major-axis is horizontal. The associated compass, which points North by East, illustrates the rotation of the data (see Table 1 for adopted position angles). The panel below the contour map plots the locations of each measurement used to construct the kinematic maps and includes the 1 R_e contour and the convex hull (bounding polygon) of data locations.

In the smoothed kinematic maps shown at right, each measurement is assigned a Voronoi bin (see previous section) and plotted as a function of X and Y position in the galaxy, normalized by effective radius. Panels are labeled according to measurement type (V, σ, h_3, or h_4), and Voronoi bins are colored according to value using the colorbar shown at bottom-left. The minimum/maximum of the range is printed in the bottom right corner of each panel.

2.6 Multi-Component Structure of ETGs

A number of recent studies find evidence for significant size growth in massive ETGs between $z \sim 2$ and today (e.g., Daddi et al. 2005, Trujillo et al. 2006, Dokkum et al. 2008, Buitrago et al. 2008). Galaxies selected at constant number density over this interval appear to gradually grow in size (van Dokkum et al. 2010) from the inside out (Bezanson et al. 2009). Cosmological simulations suggest this growth is a natural consequence of multiple minor mergers (Naab et al. 2009, Oser et al. 2010), which serve to build extended outer envelopes from accreted stars. In this view, ETGs have a two-component structure consisting of an inner region primarily composed of stars formed in-situ at $z = 1 - 3$, and an outer extended halo composed of material accreted over the past $\sim$10 Gyr.

Higher mass galaxies are expected to have more active assembly histories and thus contain a larger fraction of accreted stars (Oser et al. 2010) relative to lower mass galaxies. Interestingly, the amount of accreted material may be linked to whether an ETG becomes a fast

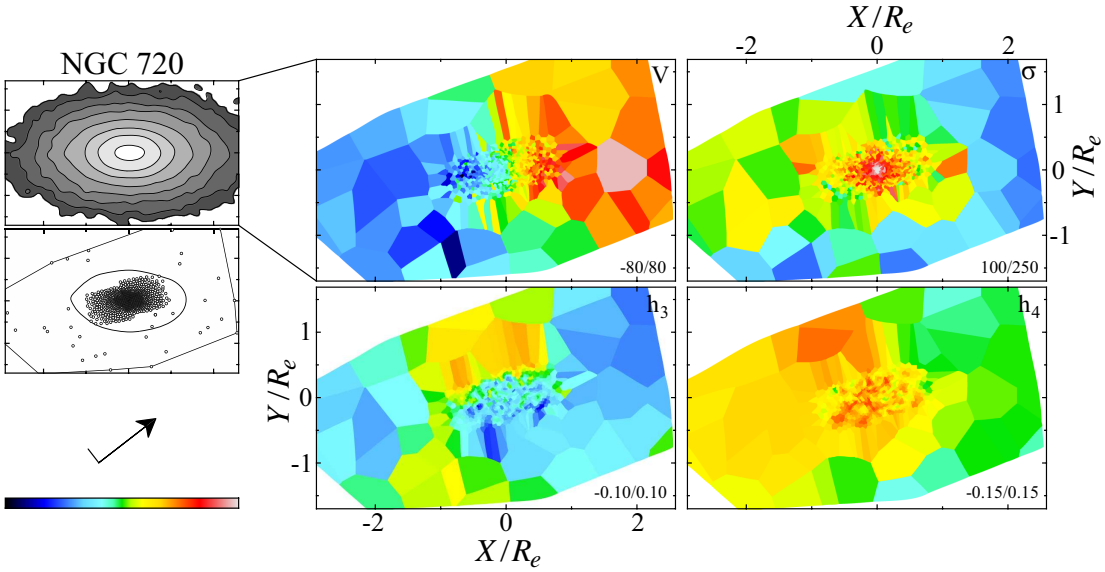

Figure 2.12: Smoothed kinematic maps for NGC 720. A separate subplot for each galaxy includes an I-band DSS image (top-left), a plot of measurement locations (middle-left), and a compass marking North and East. In the data location plot the $1\,R_e$ isophote is represented by a solid black ellipse, while each separate spectrum is denoted by a black dot surrounded by the convex hull of measurement locations (solid black polygon). Kinematic maps of V (center-top), σ (right-top), h_3 (center-bottom), and h_4 (right-bottom) are smoothed using the algorithm described in Section 2.4.1. The coloring scheme is set according to the colorbar (bottom-left), with the minimum/maximum of each range printed in the bottom right corner of each panel; V and σ are in $km\,s^{-1}$, h_3 and h_4 are unit-less. The plotted spatial scale, which varies from galaxy to galaxy, is only displayed for the σ and h_3 maps; with X and Y-axes normalized by the R_e values listed in Table 2.2. In addition to our own measurements, we incorporate IFU kinematic data from Cappellari et al. (2007).

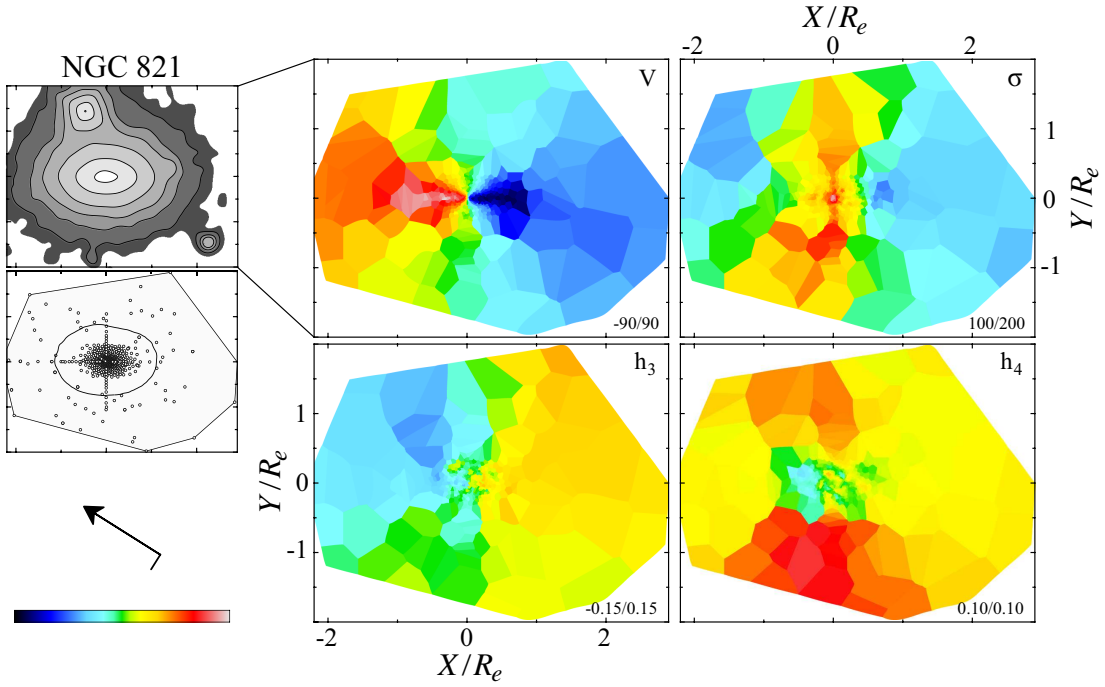

Figure 2.13: Kinematic maps for NGC 821. Layout is as in Figure 2.12, with additional literature measurements from Pinkney et al. (2003), Emsellem et al. (2004), Proctor et al. (2005), Weijmans et al. (2009), and Forestell & Gebhardt (2010).

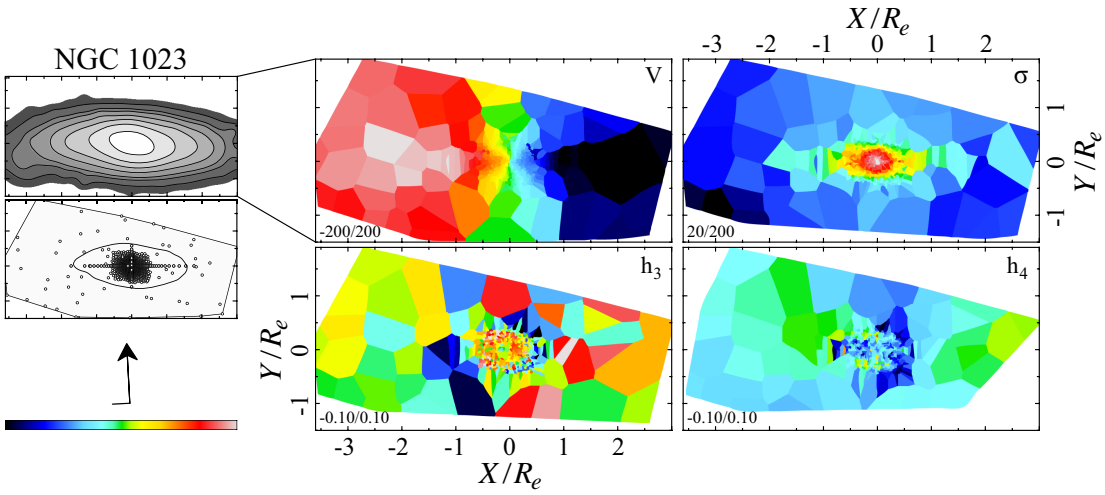

Figure 2.14: Kinematic maps for NGC 1023. Layout is as in Figure 2.12, with additional literature measurements from Emsellem et al. (2004) and Fabricius et al. (2012).

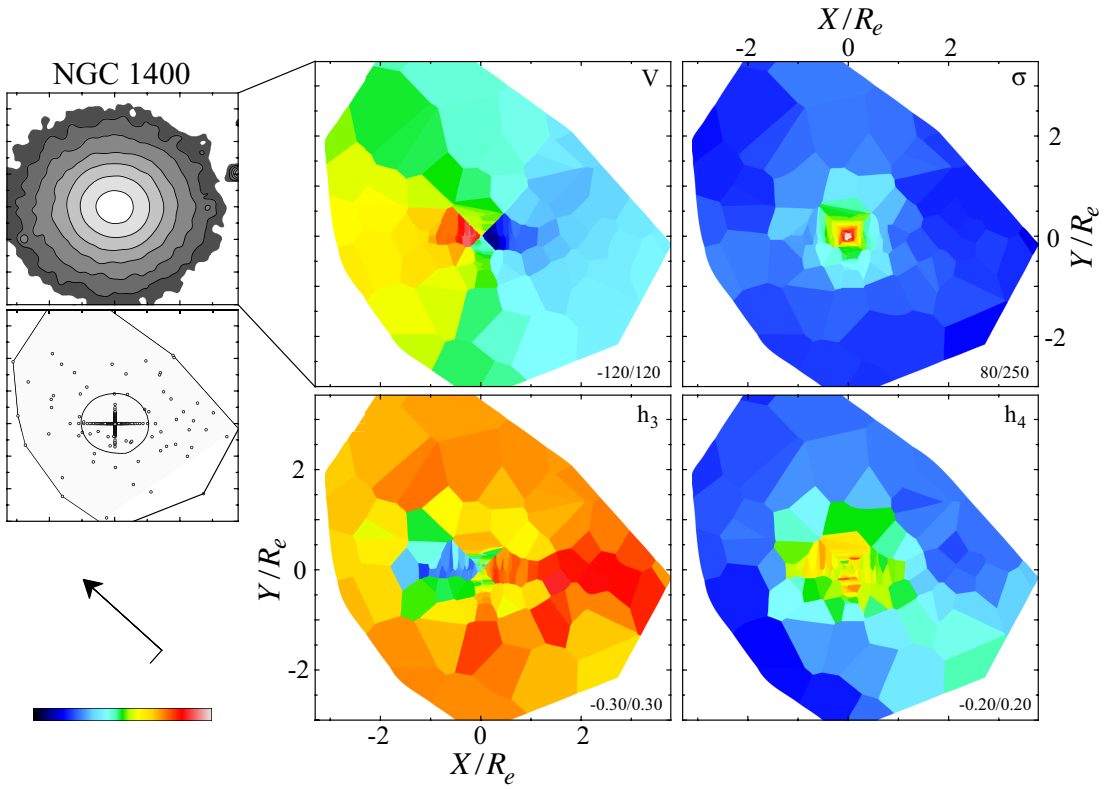

Figure 2.15: Kinematic maps for NGC 1400. Layout is as in Figure 2.12, with additional DEIMOS long-slit data and literature measurements from Spolaor et al. (2008).

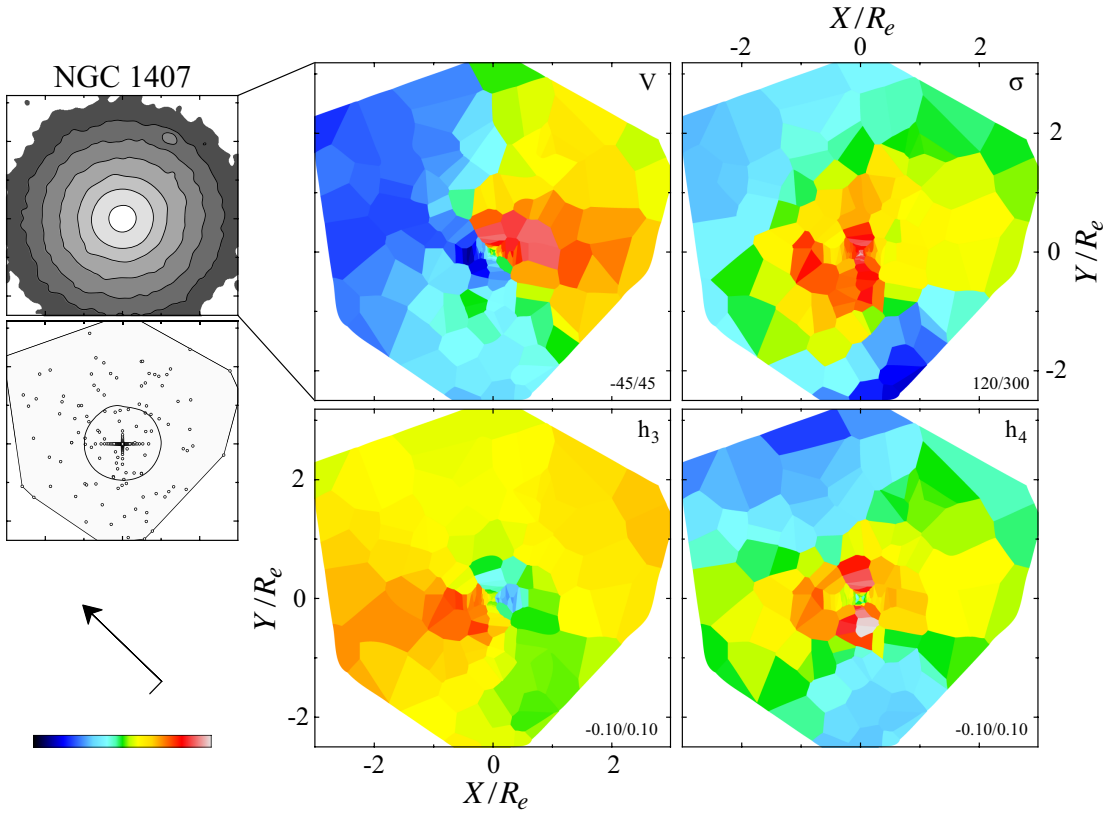

Figure 2.16: Kinematic maps for NGC 1407. Layout is as in Figure 2.12, with additional DEIMOS long-slit data and literature measurements from Spolaor et al. (2008).

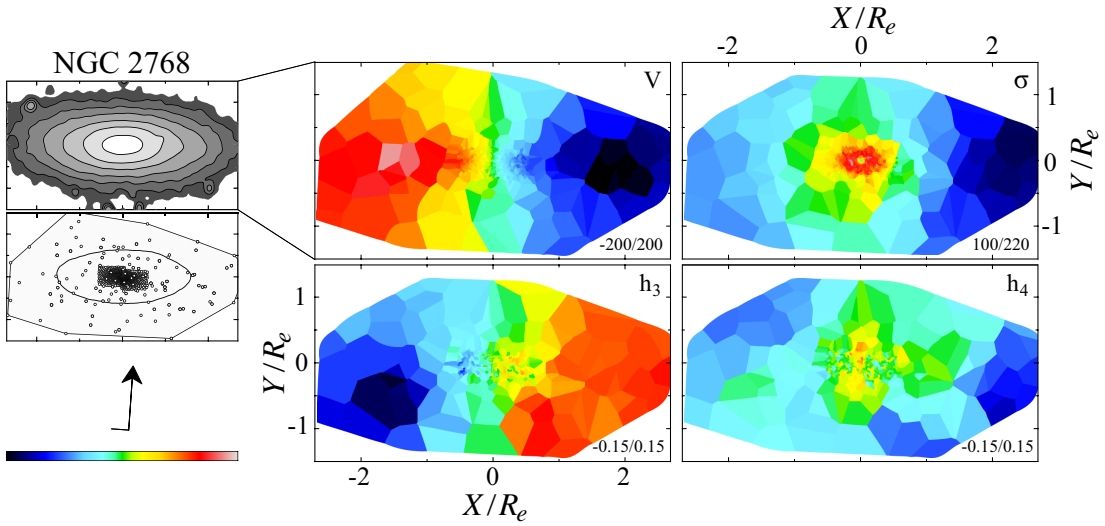

Figure 2.17: Kinematic maps for NGC 2768. Layout is as in Figure 2.12, with additional literature measurements from Emsellem et al. (2004).

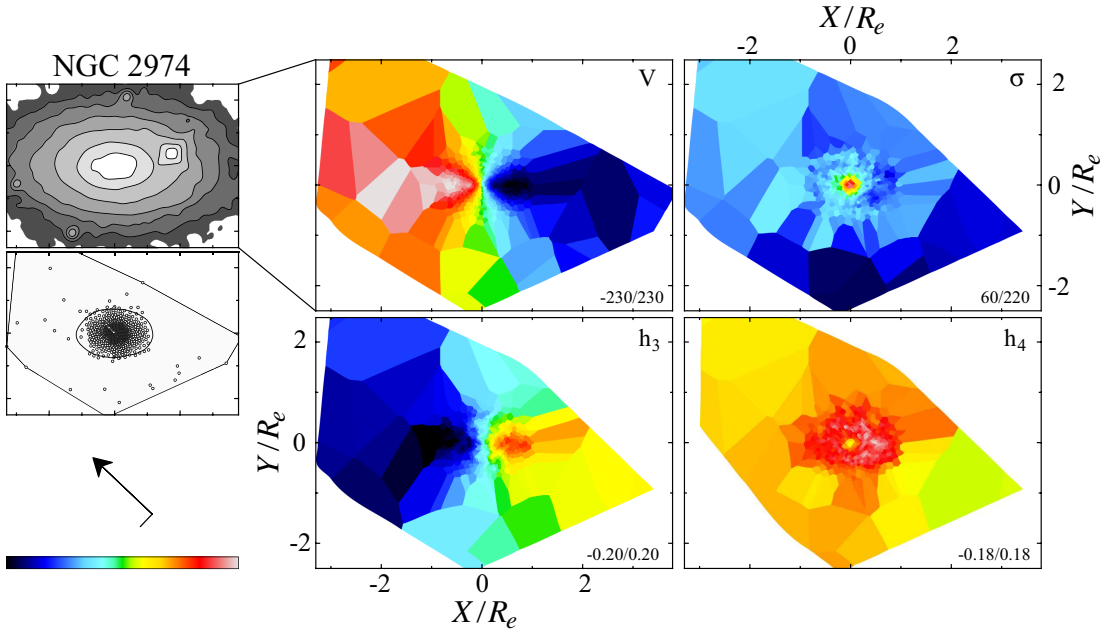

Figure 2.18: Kinematic maps for NGC 2974. Layout is as in Figure 2.12, with additional literature measurements from Emsellem et al. (2004).

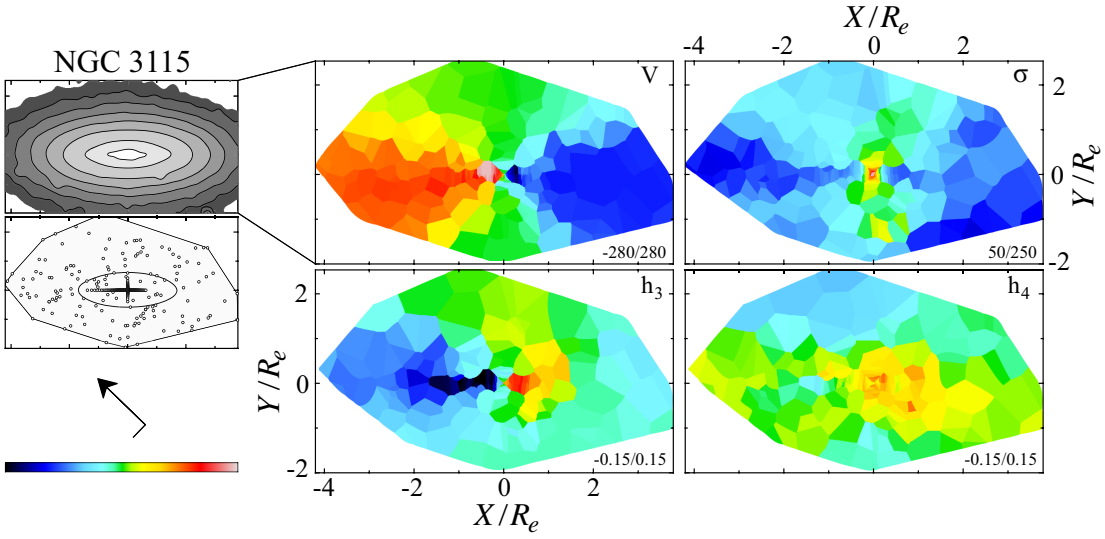

Figure 2.19: Kinematic maps for NGC 3115. Layout is as in Figure 2.12, with additional long-slit measurements from Norris et al. (2006).

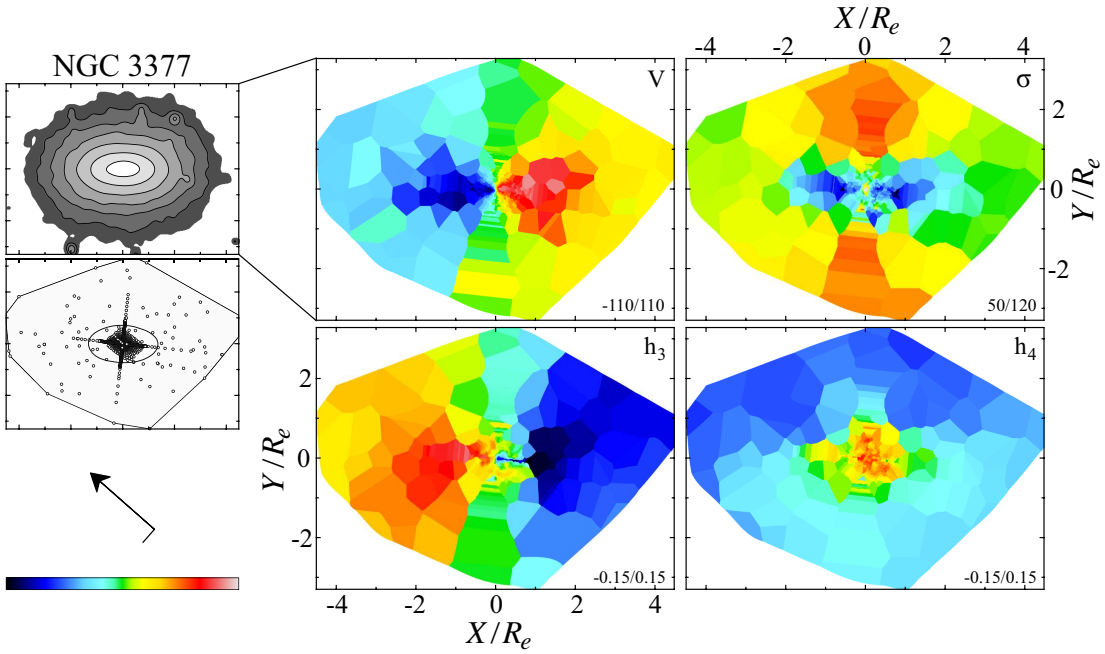

Figure 2.20: Kinematic maps for NGC 3377. Layout is as in Figure 2.12, with additional literature measurements from Emsellem et al. (2004) and Coccato et al. (2009).

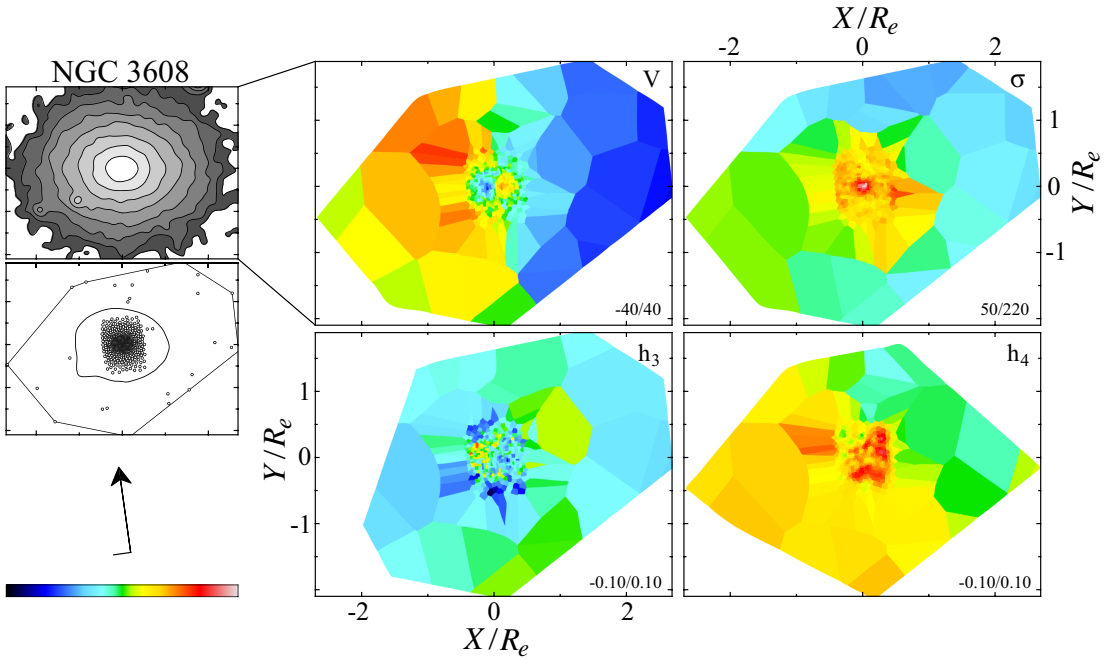

Figure 2.21: Kinematic maps for NGC 3608. Layout is as in Figure 2.12, with additional literature measurements from Emsellem et al. (2004).

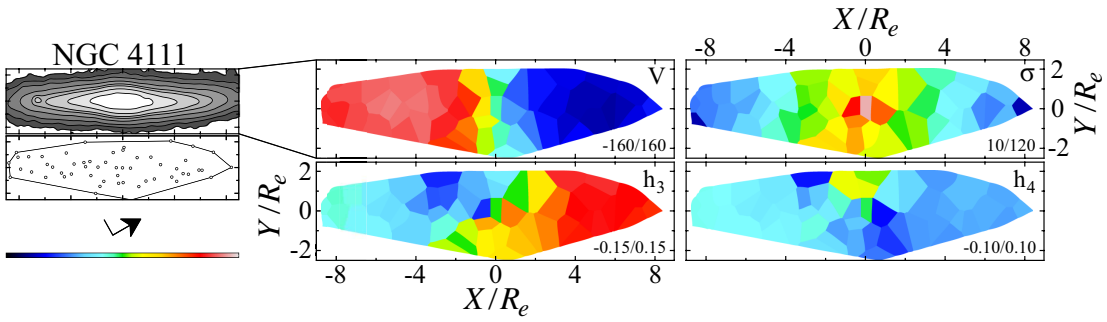

Figure 2.22: Kinematic maps for NGC 4111. Layout is as in Figure 2.12.

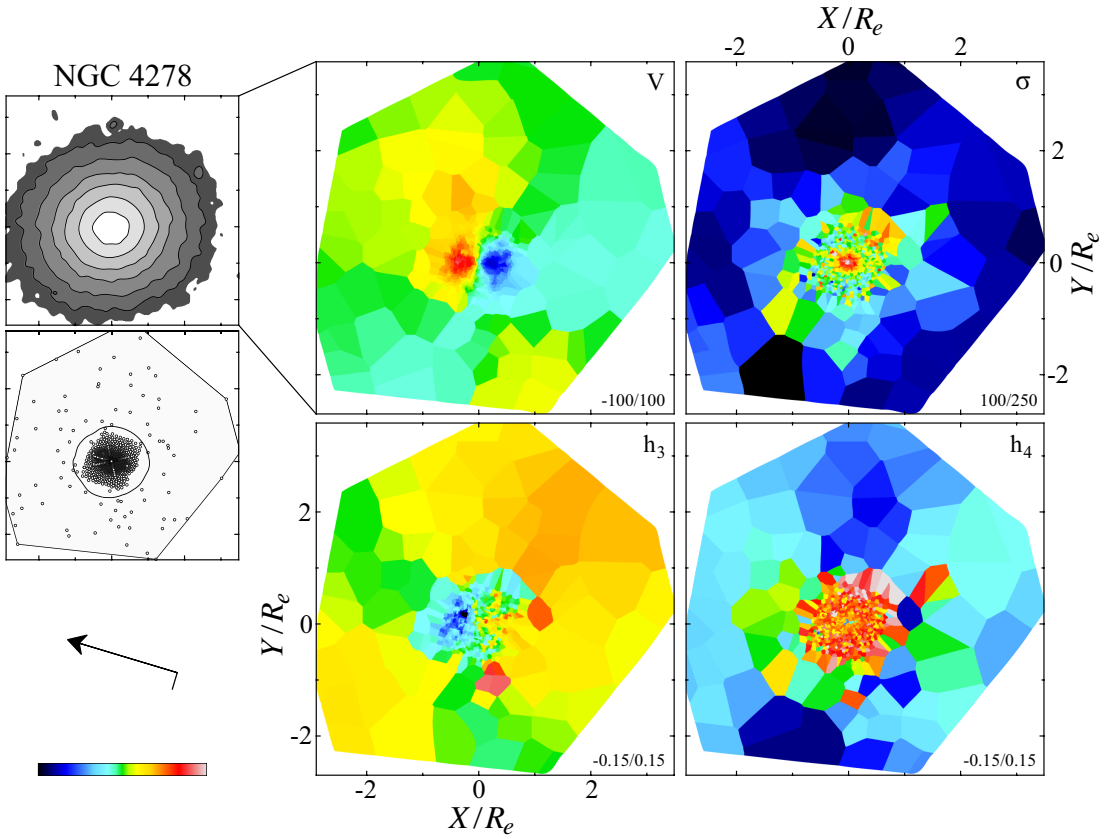

Figure 2.23: Kinematic maps for NGC 4278. Layout is as in Figure 2.12, with additional DEIMOS long-slit data and literature measurements from Emsellem et al. (2004).

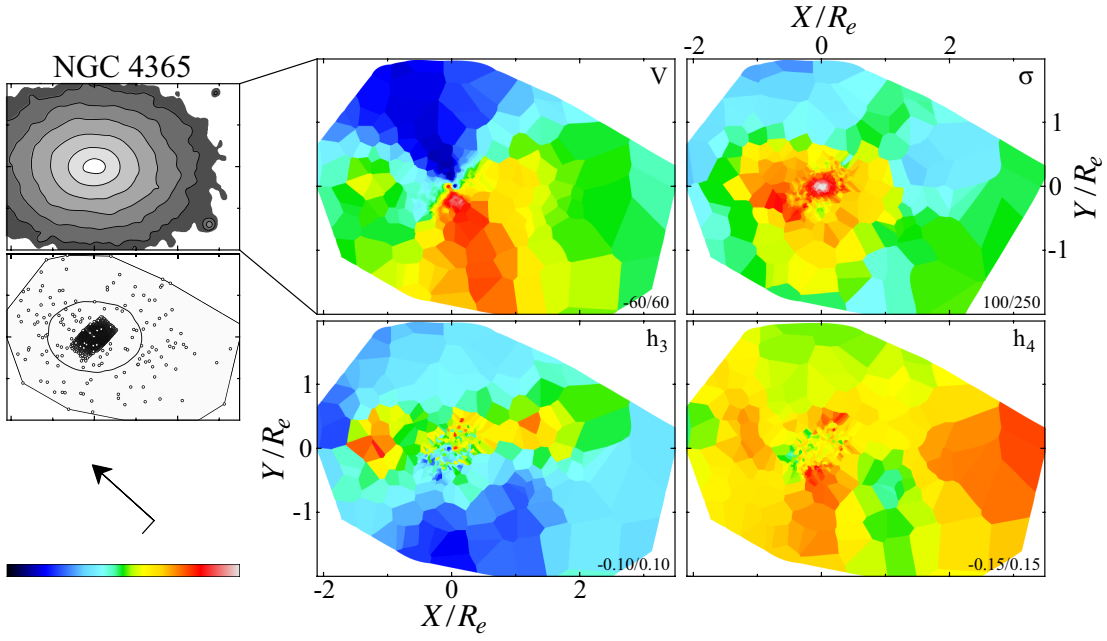

Figure 2.24: Kinematic maps for NGC 4365. Layout is as in Figure 2.12, with additional SAURON IFU measurements (Eric Emsellem: private communication) .

or slow rotator at $z = 0$ (Khochfar et al. 2011). Repeated mergers tend to erode disk structure and produce spheroids with little net angular momentum, i.e., slow rotators. The same effect occurs for fast rotators, but the amount of accretion is lower, which preserves more of the initial diskyness and allows for possible disk regrowth. Recently, Krajnovic et al. (2012) performed 1D photometric bulge-disk decompositions of the bar-less ATLAS^{3D} ETG galaxies, revealing that 83% of them contain disk-like structures. The authors combined the photometric disk-to-total ratios (D/T) with the measured kinematics within $\sim 1\,R_e$ to show that FRs have relatively more luminous disky components than SRs. Interestingly, both FRs and SRs host embedded structures, but FRs have larger D/T ratios on average while SRs show a wider range of values. This latter point is perhaps unsurprising given that SRs tend to be more massive and thus more likely to have complicated interaction histories that lead to more varied properties.

With the inside-out ETG formation pathway in mind, we envision a simple physical

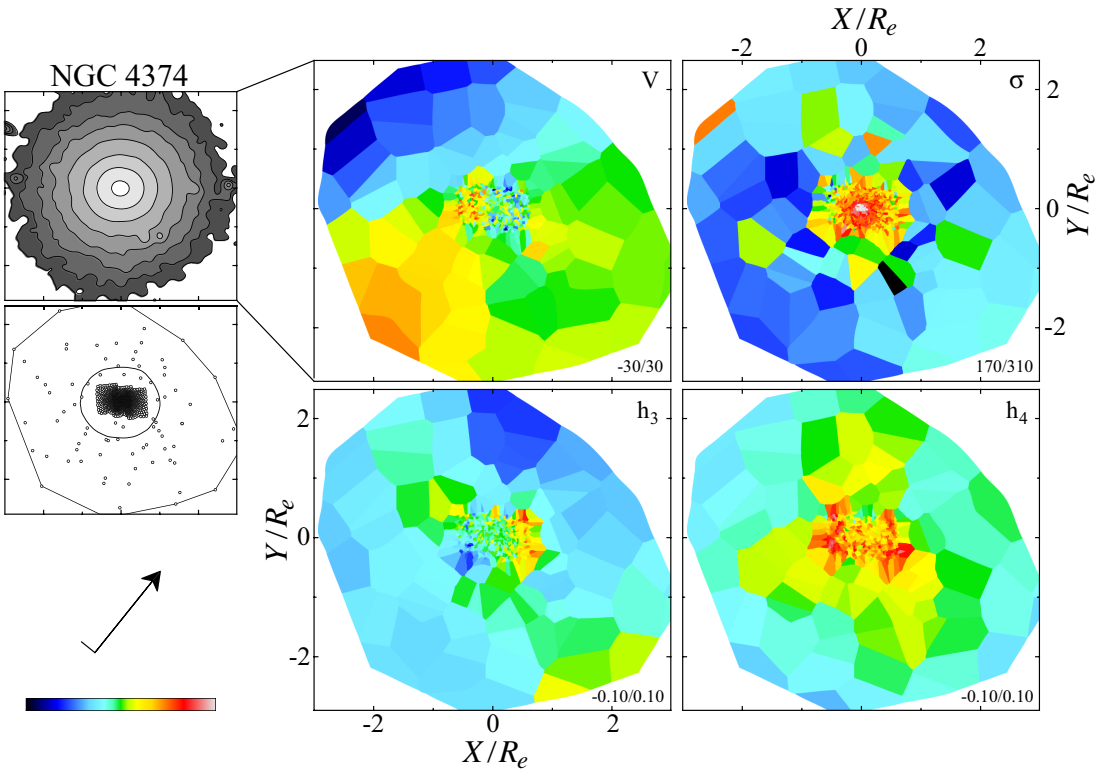

Figure 2.25: Kinematic maps for NGC 4374. Layout is as in Figure 2.12, with additional literature measurements from Emsellem et al. (2004).

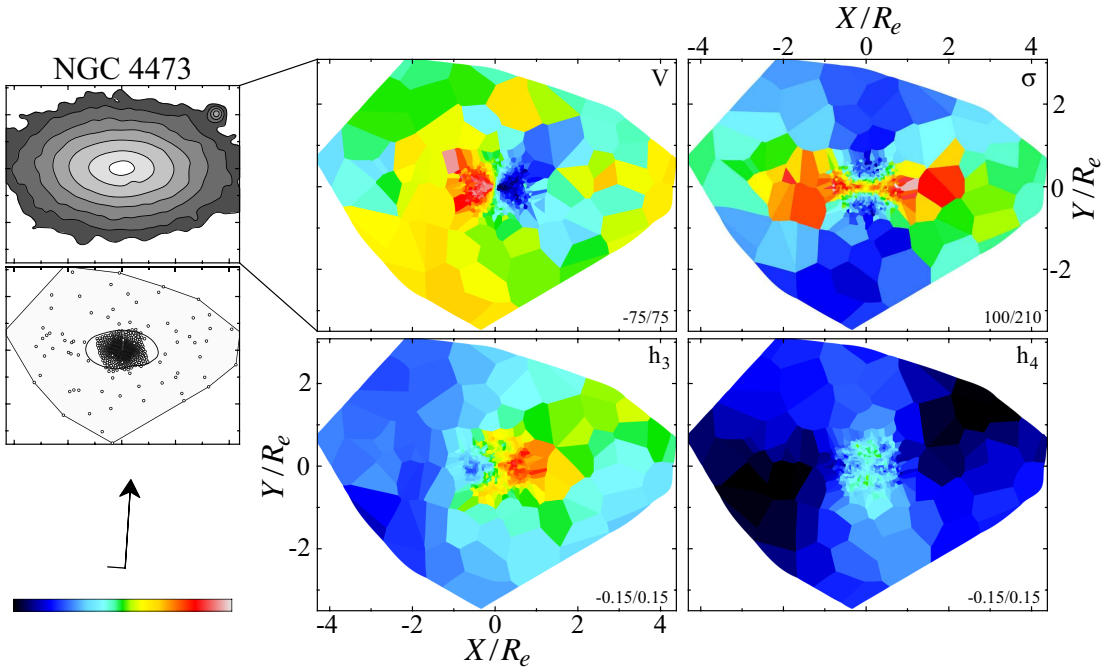

Figure 2.26: Kinematic maps for NGC 4473. Layout is as in Figure 2.12, with additional literature measurements from Emsellem et al. (2004).

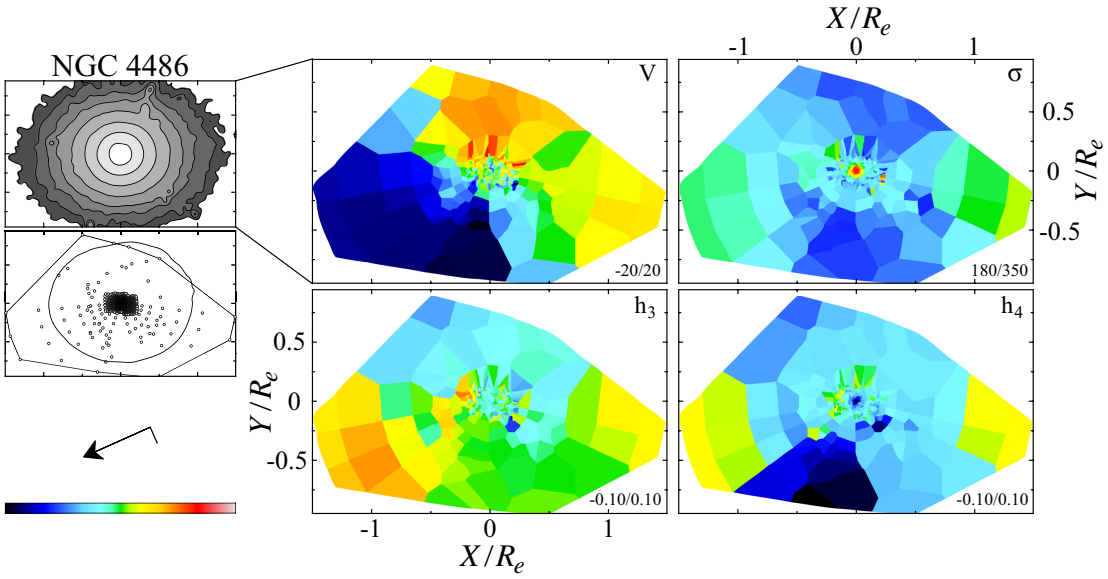

Figure 2.27: Kinematic maps for NGC 4486. Layout is as in Figure 2.12, with additional literature measurements from Emsellem et al. (2004) and Murphy et al. (2011).

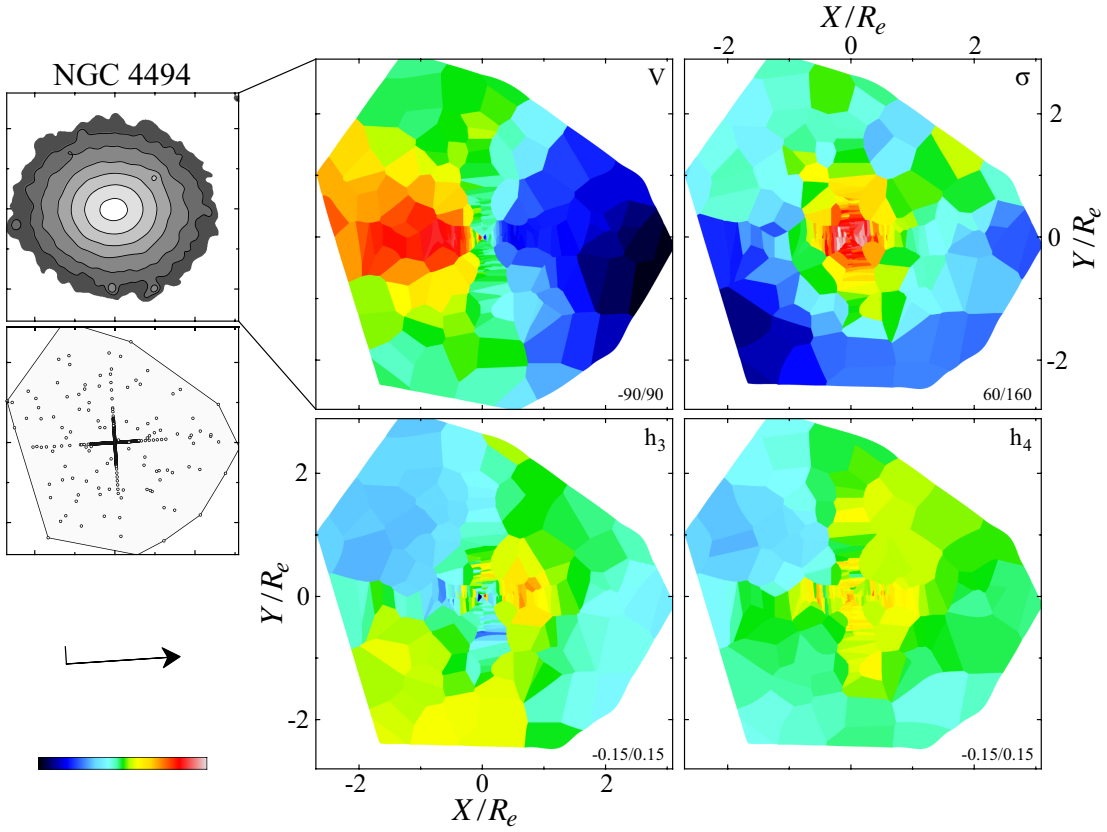

Figure 2.28: Kinematic maps for NGC 4494. Layout is as in Figure 2.12, with additional long-slit measurements from (Coccato et al. 2009).

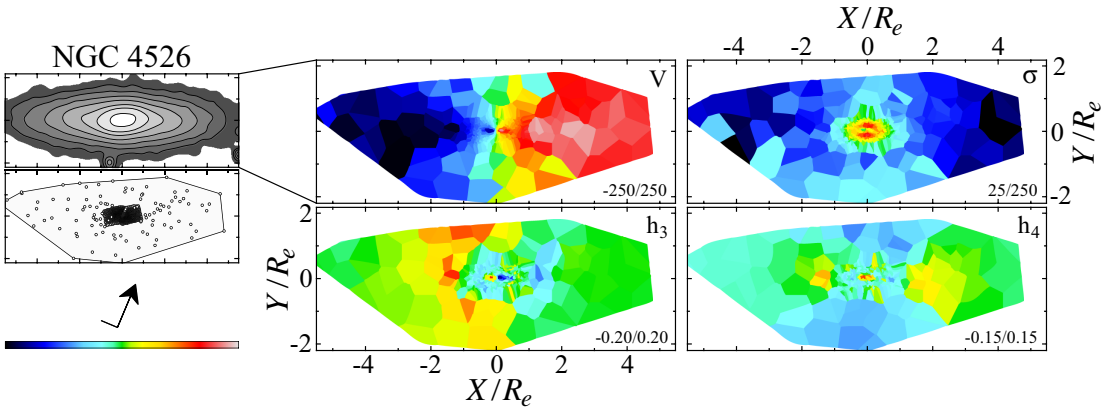

Figure 2.29: Kinematic maps for NGC 4526. Layout is as in Figure 2.12, with additional literature measurements from Emsellem et al. (2004).

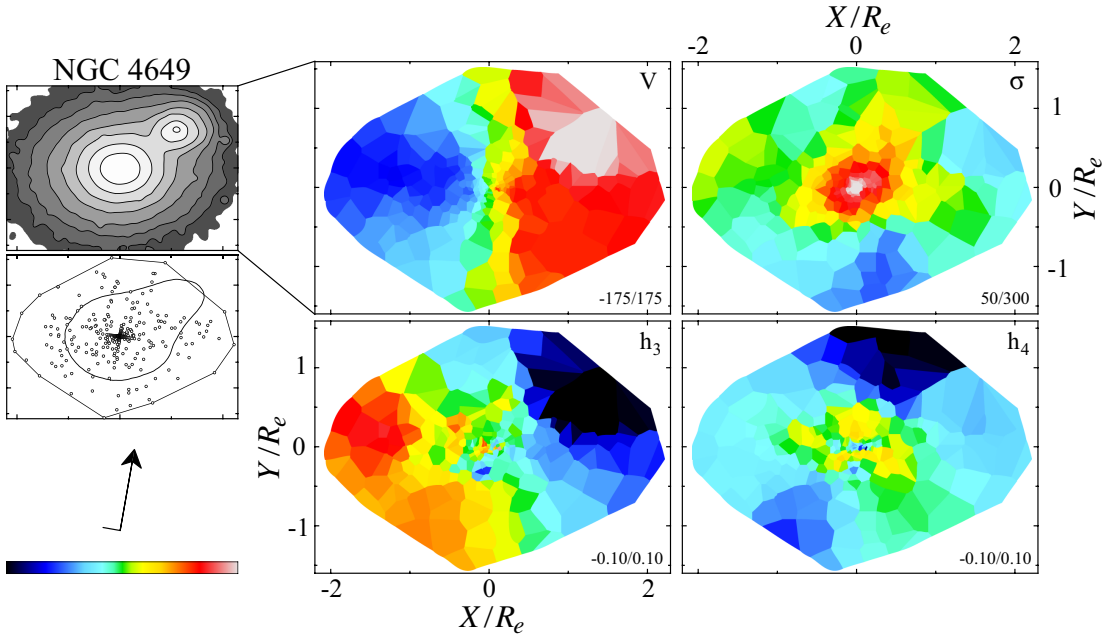

Figure 2.30: Kinematic maps for NGC 4649. Layout is as in Figure 2.12, with additional DEIMOS long-slit data and literature measurements from Pinkney et al. (2003).

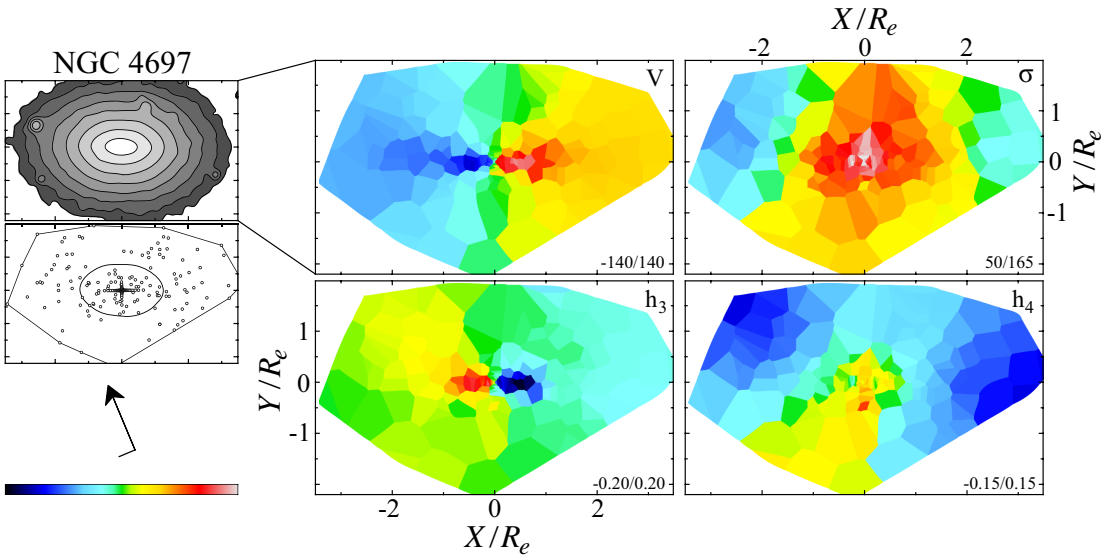

Figure 2.31: Kinematic maps for NGC 4697. Layout is as in Figure 2.12, with additional DEIMOS long-slit data.

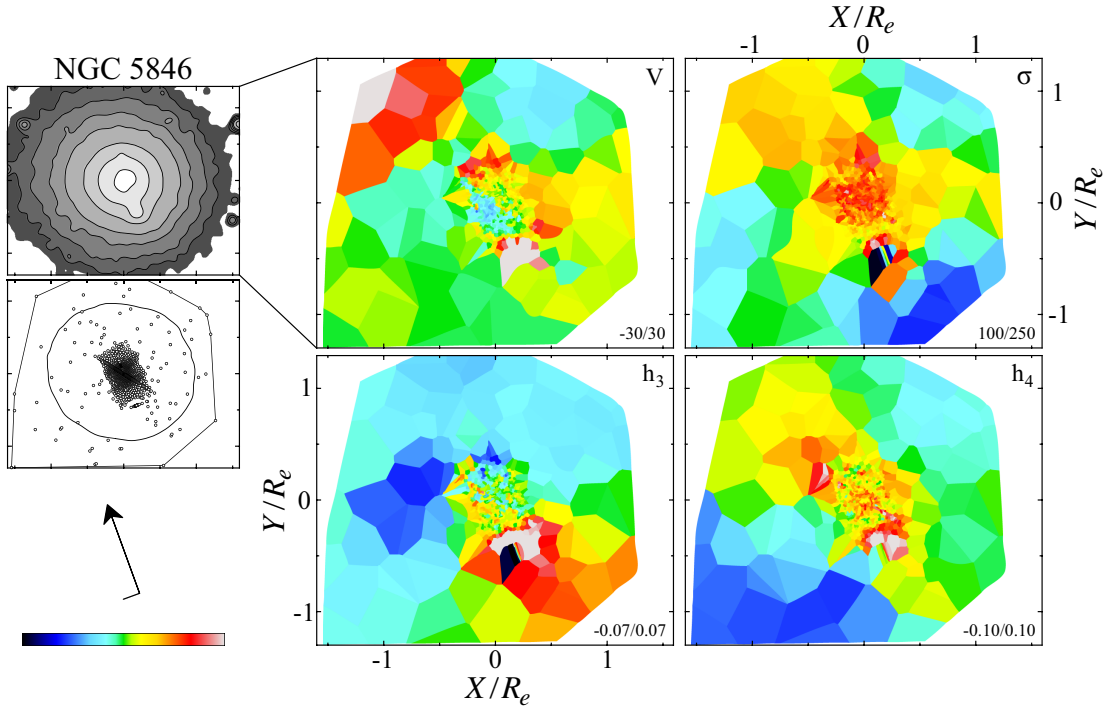

Figure 2.32: Kinematic maps for NGC 5846. Layout is as in Figure 2.12, with additional DEIMOS long-slit data and literature measurements from Emsellem et al. (2004).

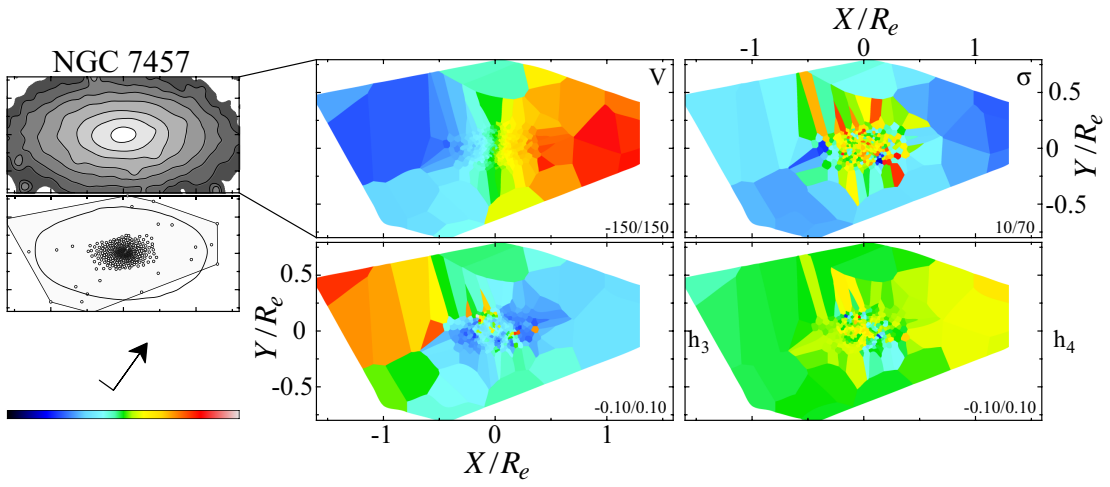

Figure 2.33: Kinematic maps for NGC 7457. Layout is as in Figure 2.12, with additional literature measurements from Emsellem et al. (2004).

picture in which an ETG is composed of an oblate rotating inner structure embedded within a more extended, spheroidal, and slowly rotating halo comprised of accreted stars. The transition radius between these two components will be different for each galaxy, but we can get a rough idea where this might occur from photometric observations between $z = 0$ and $z = 2$, which suggest significant mass growth in massive ETGs beyond a radius of 5 kpc (van Dokkum et al. 2010). For nearby ETGs, this equates to roughly $1 - 2$ effective radii. Relatively recent disk regrowth may have occurred for some of the ETGs in our sample as well, producing disky components that are kinematically similar to ancient in-situ oblate structures. In the remainder of this sub-section, we take advantage of SMEAGOL's wide-field kinematic perspective to examine the evidence for embedded disky structures on multi-R_e spatial scales. We focus on the existence of such structures and remain agnostic on their exact formation pathways, deferring such an analysis to a future paper in this series.

2.6.1 Rotational Signatures

Given that disks tend to rotate more rapidly than spheroids, we expect to see radially declining rotation as the relative surface brightness of the disk fades with increasing radius. Interestingly, 7 of the 16 FRs exhibit either a sudden or gradual decline in rotation beyond $1\,R_e$ (NGC 821, NGC 1400, NGC 3115, NGC 3377, NGC 4278, NGC 4473, NGC 4697). At least one of the remaining FRs (NGC 1023) is known to exhibit this same behavior at larger radius ($\sim 3\,R_e$) from planetary nebula kinematics (Noordermeer et al. 2008, Cortesi et al. 2011). The remaining 8 FRs have rotation amplitudes at $2 - 3\,R_e$ that are consistent with an outward extrapolation of their inner values (NGC 720, NGC 2768, NGC 2974, NGC 4111, NGC 4494, NGC 4526, NGC 4649, NGC 7457). We point out that the large scale rotation at larger radius is still reasonably well aligned with the photometric major-axis at these larger size scales, consistent with previous analyses at smaller radius that suggest axisymmetry (Krajnović et al. 2011).

The situation is less clear in the SR galaxies where prominent rotating structures on $1\,R_e$ scales are precluded by definition. However, other velocity features such as kinematically distinct cores (KDCs; e.g., NGC 3608, NGC 4365), minor-axis rotation (e.g., NGC 4365, NGC 4374, NGC 4486), and kinematic twisting (e.g., NGC 1407) are more common.

We are interested in whether the rotational structures become more or less dynamically important with radius. Figure 2.34 illustrates the relative importance of the rotation at 0.5 and $2\,R_e$. Here we plot differential λ_{R_e}, with the value determined in an annulus rather than as a cumulative sum out to a particular radius (Emsellem et al. 2007). In this form, $\lambda(R = r)$ is similar to $V/\sigma(R = r)$ in that it captures the relative importance of rotation to dynamical structure at a radius r. We plot the difference in this quantity between 0.5 and 2 R_e versus the value at 1 R_e. Values on the vertical axis above zero are systems where rotation becomes more dominant with radius, while values below zero exhibit declining rotation with increasing radius. The points are colored according to 2MASS K-band magnitude, with the sizes reflecting the relative effective radii. The shape of the points reflects the photometric ellipticity from Table 1. The vertical dashed line denotes an approximate division between fast and slow rotators. The galaxies toward the bottom of the plot are those with obvious embedded disk structures (NGC 821, NGC 1400, NGC 3377). NGC 3115, which is above 0, also has a fairly obvious edge-on disk, but is embedded in a dominant fast rotating bulge. So, on these spatial scales, rotation is more dynamically important with radius except in those systems where the embedded structure is fully resolved. However, based on even larger scale discrete velocity measurements of globular clusters and planetary nebulae, we expect that some of the galaxies would move to the bottom of the plot (e.g., NGC 3115, NGC 1023).

The galaxies presented here do not comprise a volume limited sample, so we cannot definitively comment on the fraction of ETGs with rapidly rotating inner structures. However, it is clear from the above results that steep rotational drops are fairly common on $2 - 3\,R_e$

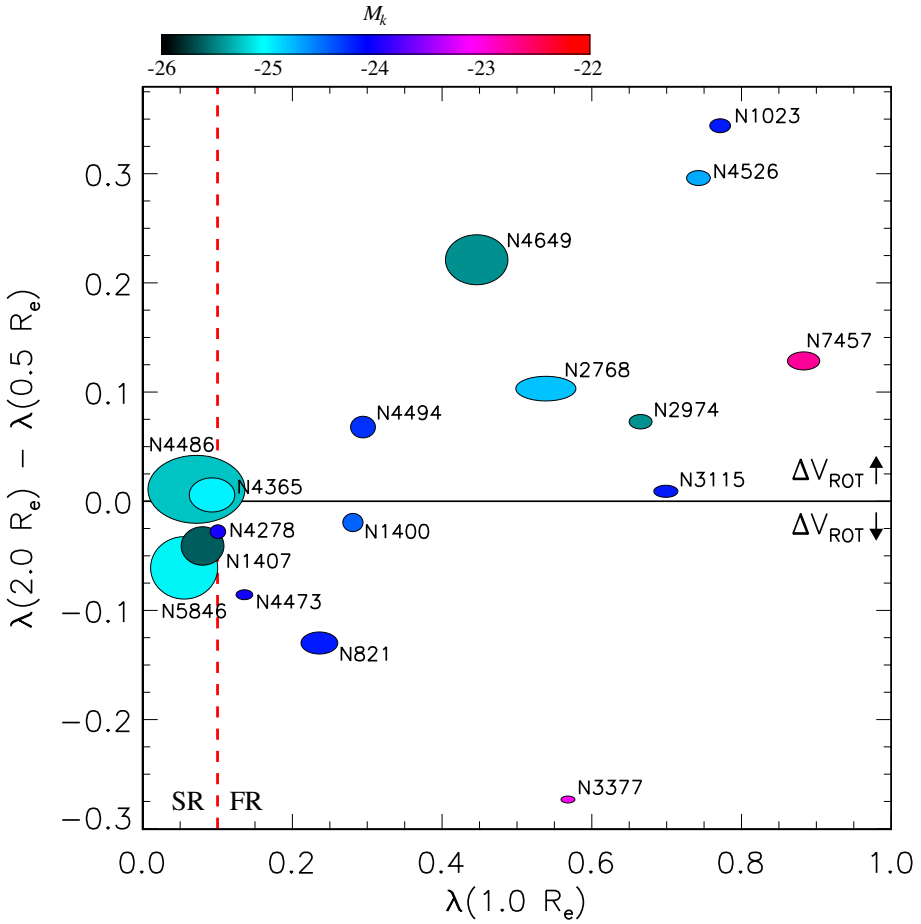

Figure 2.34: The radial dependence of angular momentum. Most of the galaxies in our sample show an increase in differential specific angular momentum (parameterized as $\lambda(R = r)$) with radius. The difference between each galaxy's $\lambda(R = r)$ at 2 R_e and 0.5 R_e is plotted versus each galaxy's $\lambda(R = r)$ value at 1 R_e. Each point is sized according to galaxy effective radius (in physical units) and is to scale, while the shape and color reflect isophote shape at 1 R_e and absolute K-band magnitude, respectively. A fiducial division between fast and slow rotators is shown as a red horizontal dashed line. Fast-rotator (FR) galaxy's with $\Delta\lambda_{0.5,2} = \lambda(R = 2R_e) - \lambda(R = 0.5R_e)$ values above 0 show increasing rotation beyond 0.5 R_e. Conversely, FR galaxy's with $\Delta\lambda_{0.5,2}$ below 0 tend to have radially decreasing rotation profiles generally indicative of small embedded disks.

spatial scales. This in turn supports the notion that embedded disks are common in FR ETGs insomuch as they are associated with sudden declines in rotation.

2.6.2 $V/\sigma - h_3$ anti-correlation

Another classic indicator of embedded disks within ETGs is the Gauss-Hermite h_3 moment, which is a measure of skewness in a LOSVD. V/σ and h_3 are frequently anti-correlated in ETGs (e.g., Bender et al. 1994, Krajnović et al. 2008), indicating an extended tail of stars in the direction of the galactic systemic velocity. This is sometimes interpreted as evidence for an embedded fast rotating disk within a more slowly rotating bulge (Rix & White 1990, Scorza & Bender 1995) since projection effects are incapable of producing the amplitude of the anti-correlation in dispersion dominated galaxies (Bender 1990). Interestingly, simulated ETG remnants resulting from dissipationless major-mergers tend to have correlated rather than anti-correlated $V/\sigma - h_3$ values (Bendo & Barnes 2000, Cretton et al. 2001, Naab & Burkert 2001). This can be understood as a consequence of a triaxial core forming in these remnants, which can occur in the absence of dissipation, leading to stable box orbits and correlated $V/\sigma - h_3$ values. Conversely, hydrodynamical simulations of dissipational gas-rich mergers produce remnants that are more oblate, and hence do not support box orbits. In these simulations, the conversion of box into tube orbits with no preferred rotation vector plus the ability to rebuild a disk post merger leads to anti-correlated $V/\sigma - h_3$ values. The implication is that dissipation plays a key role in determining the internal kinematic structure of ETGs, and by extension, in shaping their LOSVDs.

In our sample all of the FR galaxies with embedded disky structures identified by their rapid rotation in the previous section have anti-correlated $V/\sigma - h_3$ values in the same region. The same is true for at least one SR galaxy – the massive BCG NGC 1407 has a rotating structure within $1\,R_e$ that is misaligned with the photometric major-axis and exhibits

clearly anti-correlated $V/\sigma - h_3$. These observations support the claim in the previous section that these rapidly rotating inner structures are actually embedded disks within slowly rotating stellar spheroids.

A natural expectation might be that V/σ and h_3 remain anti-correlated in an ETG only in the region where there is a relatively massive embedded disk. However, the $V/\sigma - h_3$ anti-correlation is also evident on larger scales in regions where there is no obvious fast rotating or disky embedded component (see e.g., NGC 821, NGC 2768, NGC 3377, NGC 4697). This may indicate that a second rotation drop will occur at sufficiently large radius. The implication is that ETGs are poly-component systems, with multiple layers of embedded structure (see e.g., Arnold et al. 2011).

As an interesting side note, we point out the kinematics of the FR barred S0, NGC 1023. Empirically, barred fast-rotator galaxies tend to show a mix of $V/\sigma - h_3$ correlation and anti-correlation (Krajnovic et al. 2012). NGC 1023 is no exception with h_3 amplitudes that remain low and oscillate between correlation and anti-correlation (e.g., Debattista et al. 2002). The interesting aspect here is that NGC 1023 is thought to have a kinematically distinct rapidly rotating disk and slowly rotating bulge (Cortesi et al. 2011) which would usually equate to strongly anti-correlated $V/\sigma - h_3$.

2.6.3 σ and h_4

If the physical picture is of a flattened rotating structure embedded within a dynamically hotter and more slowly rotating spheroid, then a natural expectation is for reduced/increased velocity dispersion along the major/minor-axes of ETGs when viewed close to edge-on. On the major-axis, the contribution of a colder diskier structure will decrease the measured velocity dispersion. Conversely, on the minor-axis, the spheroid will dominate and its hotter dynamics results in large velocity dispersion values. Unambiguous instances of this

σ behavior are observed in the maps for NGC 821, NGC 3115, NGC 3377, and NGC 4526. Notably, all four of these galaxies also exhibit highly structured h_4 maps with a range of both positive and negative amplitudes.

The elliptical NGC 4473 is noteworthy for being one of the few galaxies in the original SAURON survey with a radially decreasing rotational amplitude accompanied by an increasing velocity dispersion along the major-axis. This behavior is understood as a consequence of tangential anisotropy arising from two co-spatial counterrotating disks (Cappellari et al. 2007). At larger radius this trend continues (see Figure 2.12), with the rotation eventually becoming retrograde at $\sim 3\,R_e$ (see also Foster et al. 2013). The negative h_4 amplitudes near the major-axis (see also Emsellem et al. 2004) bolster the case for tangential anisotropy (e.g., van der Marel & Franx 1993).

2.7 Concluding Remarks

We have presented wide-field ($> \ 2\,R_e$) kinematic maps of V, σ, h_3, and h_4 for 22 nearby early-type galaxies. Our sample consists of 16 fast rotators and 6 slow rotators – close to the observed fast rotator fraction measured in the volume limited sample from ATLAS^{3D}(86%; Emsellem et al. 2011). These galaxies span a range of sizes (0.8–8.6 kpc), ellipticities (0.04–0.58), luminosities ($-22.4 < M_K < -22.6$), morphologies (S0–E0), and environments (Field, Group, and Cluster). Given this diversity of properties, it is perhaps unsurprising that these galaxies also exhibit a range of large scale kinematic behaviors (see Figure 2.12).

The wealth of structure evident in these large-scale kinematic maps will require detailed dynamical modeling to fully understand and interpret within the context of ETG assembly. Here, our goal was to present this novel wide field kinematic perspective for a large sample of ETGs, and to highlight a few interesting and relatively general trends in the data. Future papers in

this series will characterize and explore the interesting structures shown here, while the data itself will become public at the conclusion of the survey.

Chapter 3

Halo Kinematics and Metallicities in the Nearest S0 Galaxy

3.1 Introduction

The early epochs of galaxy formation and growth can be explored by two complementary approaches: direct, broad-brush observations of high redshift (z) galaxies, and detailed scrutiny of close-by systems ("near field cosmology"). Of particular importance for the latter approach are the faint outer regions. Here relaxation times are long, and subtle formational clues are preserved not only in their integrated stellar light but also in bright tracer populations such as globular clusters (GCs) and planetary nebulae (PNe).

In the past, kinematic measurements of early-type galaxies (ETGs) were largely confined to the inner half-light radius (R_e; e.g., Emsellem et al. 2004). Recent advances with integrated stellar light and PNe (Proctor et al. 2009, Coccato et al. 2009) have revealed that the relative kinematic homogeneity of ETGs' central regions (Emsellem et al. 2007) gives way to more diversity in the outlying parts, e.g., central fast rotators can sometimes rotate slowly

at larger radii.

The implication is that inner and outer regions are somewhat decoupled, either from being dominated by different physical processes, or from experiencing disjoint formational histories. One possible explanation comes from the classic gas-rich binary major-merger scenario for forming galaxy bulges, where the spatial dependence of dissipational processes could produce dramatic kinematical transitions in radius (Hoffman et al. 2010).

Alternatively, inner and outer spheroids may form in two separate phases, which could explain the strong size and internal density evolution of ETGs from $z \sim 2$ to today (e.g. Daddi et al. 2005, Dokkum et al. 2008). This inside-out growth hypothesis means that the inner regions form early as compact stellar spheroids while the outer parts grow later through the accretion of smaller galaxies (e.g., Naab et al. 2009, Oser et al. 2010).

One way to distinguish between the merger and inside-out scenarios is to search for their signatures in the properties of GC systems. Born in major star-forming episodes and passively evolving for many Gyr, GCs are bright, easily identifiable tracers of early galaxy growth and ongoing accretion (e.g., Forbes & Bridges 2010, Mackey et al. 2010).

In their archetypal study, Searle & Zinn (1978) used the joint distribution of spatial, kinematical, age, and metallicity properties of GCs to infer the hierarchical buildup of the Milky Way's outer halo. A key concept here is that building galaxies via the stochastic infall of satellites leads to flattened metallicity gradients at large radius, an effect now observed within the GC systems of two ETGs (Harris 2009, Forbes et al. 2011; cf also Coccato et al. 2010). Likewise, in wet major merger remnants gas dissipation should create metallicity gradients in the central regions, with flatter profiles in the outer regions where any initial gradients have been mixed up in the merger (e.g., White 1980, Hopkins et al. 2009). The similar expectations for large-scale metallicity structure from each of these scenarios necessitates additional information, such as from kinematics, to place such results in the proper context.

A useful complication with the GCs is their bimodality, as each galaxy generally has a metal-poor and a metal-rich subpopulation (MPGCs and MRGCs). In the Milky Way these are associated with the stellar halo and the bulge or thick disk, respectively, while in ETGs there are stronger MRGC components reflecting their more dominant bulges. These subpopulations permit the investigation of two distinct phases of galaxy assembly (stellar halo and bulge) far beyond the Local Group.

As part of our ongoing surveys of ETGs we have studied the nearest giant S0 galaxy, NGC 3115 (distance 9 Mpc, inclination 86°), in unprecedented photometric and spectroscopic detail. In particular, we have obtained extensive kinematic data-sets of its field stars and GCs. Here we map out the global kinematic and metallicity structure of its dominant, extended bulge ($B/T \geq 0.9$, R_e=57"=2.5 kpc; Capaccioli et al. 1987), and examine some implications for its assembly history.

In §3.2 we describe our imaging and spectroscopic observations. Kinematic and metallicity profiles are presented in §3.3. We discuss how these results constrain the formation mechanisms of the outer bulge and halo in § 3.4, and summarize the conclusions in § 3.5.

3.2 Observations

We obtained *gri* images with 0.5″–0.7″ seeing using Suprime-Cam on the 8 m Subaru telescope. Sections of this imaging are shown in Figure 3.1a,e to provide orientation for the spectroscopic measurements discussed below. The photometry allows us to select GC candidates for follow-up spectroscopy and to characterize the distributions of number density and metallicity for the GC system. Color is used as a proxy for metallicity since GCs are generally old (see Brodie & Strader 2006, Kuntschner et al. 2002). The color boundary we use for MPGCs/MRGCs in NGC 3115 is $(g-i)_0 = 0.91$ ([Fe/H] = -0.8).

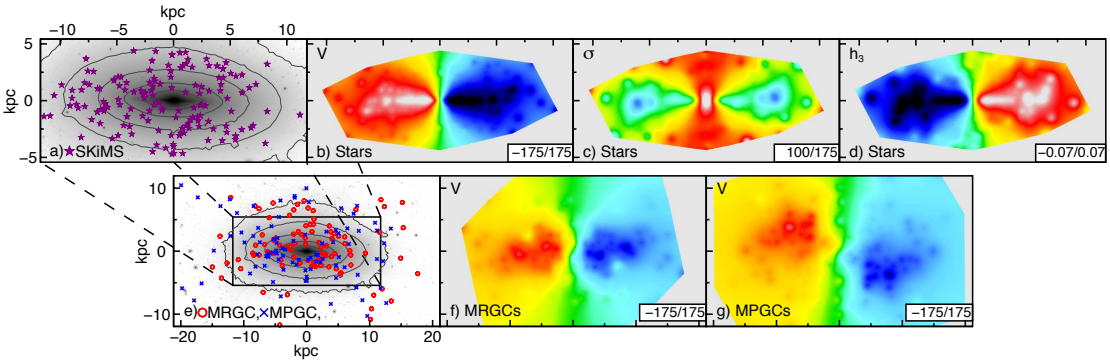

Figure 3.1: Spatial and kinematic maps of NGC 3115. Top: i-band image (a) with SKiMS (stellar light) measurement locations (purple stars). Maps of stellar rotation (b), velocity dispersion (c) and h_3 (d), each sharing the same spatial scale as (a). Bottom: Zoomed-out view (e) with spectroscopically confirmed metal-rich (red circles) and metal-poor GC (blue crosses) locations. The inset rectangle denotes the region shown in (a) where selected i-band isophotes are also overplotted. Rotation maps, made using the MRGC (f) and MPGC (g) datasets, with the same spatial scale as (e). The kinematic maps were created by doubling each dataset using two-point symmetry folding, replacing each value with the distance-weighted mean of its 20 nearest neighbors (for the GCs only) and then interpolating between values. The minimum/maximum color-bar scaling is recorded in the bottom right corner of each panel (all in units of km s^{-1} except for (d)). These maps are meant to reveal the broad-brush behavior of each kinematic data-set. Any small-scale structure or kinematic twisting in these maps should not be over-interpreted since these features are sensitive to sampling statistics.

We carried out spectroscopy using DEIMOS on the Keck II telescope to focus on the calcium triplet region (∼8580 Å). We have confirmed 150 GCs and also obtained spectra of the background galaxy light in 166 slits for use in a novel technique called "SKiMS" (Stellar Kinematics from Multiple Slits: Proctor et al. 2009, Norris et al. 2008). Another 15 and 11 unique GC spectra were obtained using LRIS (∼3500–7500 Å) and IMACS (∼4000–7000 Å), on the Keck I and Magellan telescopes, respectively.

GC velocities were measured by cross-correlating their absorption line spectra with stellar templates; MILES SSP templates/stars (Sánchez-Blázquez et al. 2006, Vazdekis et al. 2010; for IMACS and LRIS) or our own velocity standards (for DEIMOS). The fainter SKiMS spectra were coadded to reach a target S/N of 25 using the Voronoi 2D-binning method by Cappellari & Copin (2003). The stellar line-of-sight velocity distribution of each spectrum was parameterized as a truncated Gauss-Hermite series (V, σ, h_3, h_4) using pPXF (Cappellari & Emsellem 2004) and 13 template stars, with parameter uncertainties estimated using Monte Carlo modeling of data-sets with added noise.

Our SKiMS catalog is supplemented with long-slit stellar kinematics data from Norris et al. (2006) and Illingworth & Schechter (1982). We also incorporate 20 GC velocities from previous studies (Kuntschner et al. 2002, Puzia et al. 2004, Puzia & Sharina 2008) .

3.3 Results

Figure 3.1 shows smoothed two-dimensional maps of the data, combined with literature values as summarized in the caption. In the top row, the thin disk is evident as a narrow stripe ($< 1.6\ R_e$) within an extended bulge which rotates rapidly out to $\sim$2 R_e. The thin disk's lowered velocity dispersion, and anti-correlated V and h_3, extend well into the bulge, suggesting an additional embedded component like a very thick disk. On larger scales (Figure 3.1, bottom

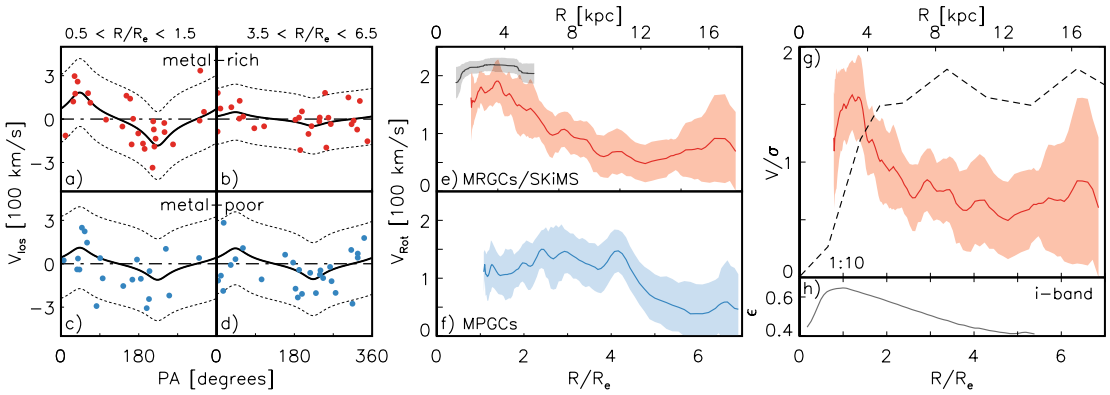

Figure 3.2: Rotation models for NGC 3115. Panels (a)–(d) plot line-of-sight velocities in two radial bins ($R/R_{\rm e} \approx 1, 5$) versus position angle for MRGCs (top) and MPGCs (bottom). Solutions for rotational velocity ($V_{\rm rot}$: solid black curves) and velocity dispersion (σ) are determined for each dataset using the kinemetry method described in the text (dotted curves denote $V_{\rm rot} \pm 2\sigma$). Smoothed rolling-fit rotational profiles with uncertainty envelopes are shown for the stellar light (black curve) and MRGCs (red curve) in (e), and for the MPGCs (blue curve) in (f). In (g) the v/σ profile of NGC 3115's MRGC subpopulation (red curve) is compared against a simulated merger remnant with a 1:10 mass-ratio (dashed: Bournaud et al. 2005). (h) contains the i-band ellipticity profile.

row), distinct rotation is seen in the MRGC and MPGC subsystems, while there is a general trend for the rotation to weaken in the outer regions.

To simplify the rotation and dispersion trends into one-dimensional profiles, we use a variation of the "kinemetry" technique developed for the SAURON survey (Krajnović et al. 2006) as optimized for data with discrete spatial and velocity sampling (Proctor et al. 2009, Foster et al. 2011). This method samples the kinematic field (e.g., rotation) using concentric elliptical annuli, and fits the data to flattened sinusoidal models as a function of position angle. For the discrete velocity data (GCs), rotation and dispersion are fitted simultaneously through a maximum likelihood method (Figure 3.2a–d). The position angles and ellipticities of the rotation field and the sampling bins ($\rm PA_{kin}$, $\epsilon_{\rm kin}$) are part of the fit for the SKiMS data but are not well constrained for the discrete velocity data, which we assume follows the stellar isophotes (PA=43.5°, ϵ=0.5). Our results turn out to be insensitive to reasonable variations in these

parameters. Uncertainties are estimated via Monte Carlo fitting of mock data-sets.

The resulting rotation profiles for the different subcomponents are shown in Figure 3.2e and 3.2f, where rolling fits with radius are used to capture the details of any radial kinematic transitions (e.g from the inner to outer bulge/halo). Within $\sim 1.5\ R_{\rm e}$ the MRGC system rotates nearly as rapidly as the stellar bulge, supporting the coevolution of these two components, as also inferred from their similar ages and metallicities (Norris et al. 2006). At larger radii, this rotation decreases dramatically (see also Figure 3.2a,b). The MPGCs have moderate rotation with a decline outside $\sim 4R_{\rm e}$.

An alternative rotation profile for the MRGCs is shown in Figure 3.2g, after normalizing by the local velocity dispersion. The photometric ellipticity profile is also plotted, showing a decrease with radius that parallels the rotational gradient. The overall implication is for a bulge that has a high degree of rotational flattening in its central regions, while becoming rounder and dispersion-dominated in its outskirts.

Having found kinematic transitions in both GC subpopulations, we look for analogous transitions in the radial metallicity profiles. First we summarize the overall color distribution of the GCs in Figure 3.3a, which shows a classic bimodality. We will assume that this bimodality persists to large radii, but that the location of the color peaks may shift. At large radii we must cope with the contaminating effects of foreground stars, whose color distribution we also show in Figure 3.3a, and use to construct Monte Carlo mock datasets to iteratively correct for the contaminant bias on the color peak locations.

Figure 3.3c shows color versus radius, both for individual GC candidates and for the fitted peak locations. Both GC subpopulations have radially-decreasing colors, which we quantify as power-law color gradients with slopes of -0.05 and -0.07 for MPGCs and MRGCs, respectively. Using our own empirical calibration to the $(g-z)$ color used in ACS surveys (Peng et al. 2006), the gradients are -0.07 and -0.10. Converting to [Fe/H] metallicity (Peng et al.

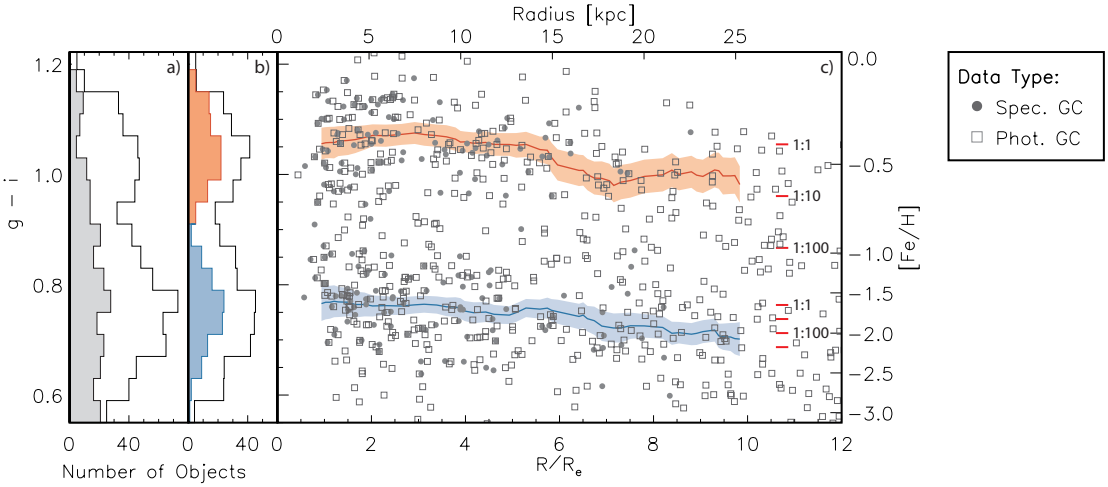

Figure 3.3: Color distributions $(g-i)_0$ of point sources around NGC 3115. Left: Overall photometrically-selected GCs (open histogram) and of stellar contaminants (filled; as measured at $R/R_{\rm e} > 14$). Middle: Resulting true GCs (open) after contaminant subtraction. Also shown are the spectroscopically confirmed GCs (filled). Right: Color versus radius. Individual GCs are shown as circles according to the legend at right. Solid curves denote rolling fits of the peak color of each GC subpopulation as estimated from a combination of mixture modeling methods (Ashman et al. 1994) and an iterative Monte Carlo scheme to correct for the contaminant color-bias. Associated error envelopes reflect both statistical and photometric uncertainties. We convert the peak color difference between the inner (1–2 R_e) and outer (> 8 R_e) portions of each GC system into merger mass-ratios (see text), with sample values shown on the right-hand side.

2006), we estimate gradients of -0.38 ± 0.06 and -0.17 ± 0.04 dex per dex.

To our knowledge, this is the first time that metallicity gradients in both GC subpopulations have been measured to large radii in any galaxy besides a few very massive ellipticals (see Section 3.1). It is also one of the first cases of any galaxy type where joint rotation and metallicity gradients are observed in the halo (see also NGC 4697: Méndez et al. 2005; 2009; and NGC 4125: Pu et al. 2010).

3.4 Implications

We now consider some possible implications of the rotation and metallicity gradients for NGC 3115's assembly history. The central bulge properties are generally consistent with a standard major merger picture, with the very high amount of rotation in this case indicative of a gas-rich merger with an uneven mass-ratio (e.g., Bournaud et al. 2005, Naab et al. 2006). Alternatively, the inner bulge might have formed via the inward migration of giant star forming clumps within a turbulent disk fed by cold streams from the cosmic web at early epochs (e.g., Noguchi 1999, Elmegreen et al. 2008, Dekel et al. 2009). In either case, the exceptionally high inner-bulge rotation in NGC 3115 may require a residual thick disk component (cf. Cretton et al. 2001, Wuyts et al. 2010). Also, the survival of an old thin disk (Norris et al. 2006) means that most of the action in the central regions occurred before $z \sim 0.65$, and that there have been no major mergers more recently.

In the outlying regions, there are generic expectations from major mergers for rotation profile behavior. These remnants are generally expected to have rapid outer rotation resulting from both residual disk spin and the conversion of orbital into internal angular momentum (e.g., Bendo & Barnes 2000, Cretton et al. 2001), in stark contrast to the declining outer rotation observed in NGC 3115. To make this difference more explicit, we have searched through the literature for extended rotation profiles from simulations of major merger remnants, choosing a representative example that comes close to reproducing the central rotation of NGC 3115's bulge and MRGC system. The chosen remnant is the result of a 1:10 spiral-spiral merger from Bournaud et al. (2005), which we overplot in Figure 3.2g, showing the discrepancy in the outer regions between the high rotation predicted and the low rotation observed.

Gas-rich 1:1 merger remnants with small pericenters can also produce declining outer rotation, but the outer "dry" part of the remnant is generally expected to show kinematical mis-

alignment with the inner regions (Hoffman et al. 2010; and in preparation). Possible examples of this scenario include NGC 5128 (Peng et al. 2004) and NGC 4125 (Pu et al. 2010), but other cases like NGC 3115 with decreasing but well-aligned rotation suggest there must be another explanation (cf. NGC 821 and NGC 3377: Proctor et al. 2009; Coccato et al. 2009; and early arguments along these lines by Scorza & Bender 1995).

Without exhaustive simulations of major mergers, we cannot rule out the possibility that finely tuned parameters (viewing angle, impact parameter, etc.) would reproduce the observed kinematics of such systems. Nonetheless, it seems more natural to consider a two-phase assembly scenario (Section 3.1) in which ETGs form inside-out. In this case, inner bulges form at high redshift while subsequent outer bulge and halo growth is driven primarily by dry minor-merger accretion events. The satellites fall in from many different directions and provide little net rotational support (Vitvitska et al. 2002, Abadi et al. 2006, Bournaud et al. 2007). The radial decline in rotation of the MRGC system could then represent a transition from an inner bulge formed in violent, dissipative processes at high redshift, to an outer spheroid (around one third of the bulge mass in the case of NGC 3115) built largely from accreted material over a more protracted period.

The MPGCs also show a marked rotational decrease, albeit at a larger radius. Here the theoretical picture is less clear, but we postulate an inner metal-poor stellar halo formed in-situ at high z followed by the accretion of outer material that also creates the outer bulge (cf. Zolotov et al. 2009).

Declining metallicity profiles are expected in this two-phase assembly scenario since the lower-mass accreted systems should be more metal-poor than the central galaxy (Naab et al. 2009, Bezanson et al. 2009). As there are not yet any quantitative predictions, we adopt a schematic model where GC peak metallicities (or colors) are markers of their host galaxies' masses (or luminosities), using the known correlations between these parameters at low z (see

below). The peak GC color in the outer bulge/halo then indicates the characteristic luminosity of the accreted systems.

The color-mass relations may well evolve with time, so we take a more general approach of considering the GC color *difference* between the central and outlying regions as an indicator of the characteristic mass-ratio that assembled the outer galaxy. Using the color-mass relations from Peng et al. (2006) for the MPGCs and MRGCs separately, we then generate predicted outer GC peak colors for various stellar mass-ratios 1:x in NGC 3115, overplotting these in Figure 3.3c. For the MPGCs we find $x = 200$ ($15 < x < 2900$; the color-mass relation is shallow so this constraint is weak) and for the MRGCs we find $x = 8$ ($3< x <19$). In combination, we estimate $x \sim$ 15–20.

Very roughly, the accreted galaxies had luminosities of $\sim 5 \times 10^8 L_{B,\odot}$, equivalent to a dwarf elliptical. Such galaxies today each host $\sim$ 20 MPGCs and $\sim$ 3 MRGCs on average (Peng et al. 2008), and could therefore account for a total of $\sim$ 350 MPGCs and $\sim$ 50 MRGCs in the outer regions of NGC 3115. These numbers are different from the $\sim$ 260 and $\sim$140 GCs that we estimate NGC 3115 to have outside 2 $R_{\rm e}$, but this discrepancy is somewhat expected given the uncertainties in these calculations (including likely progenitor bias where high-z galaxies had systematically different GC populations).

As a demonstration of the ongoing accretion process, NGC 3115 does have a dwarf companion of this luminosity at 45 kpc projected distance, NGC 3115B. This galaxy hosts $\sim$ 40 GCs (Kundu & Whitmore 2001) and we estimate the dynamical friction timescale before it disrupts and adds its stars and GCs to the main galaxy to be $\sim$ 2 Gyr.

3.5 Conclusions

We have found radially-decreasing profiles of rotation and metallicity in the GC system of NGC 3115, and compared these to theoretical expectations. While the central regions were probably formed in violent, dissipative circumstances such as a gas-rich major merger, this event should have produced high or misaligned outer rotation. A more likely scenario for explaining the assembly of the outer bulge and halo is via dry minor mergers and accretion events, whose mass-ratios we have tentatively quantified via the GC metallicities.

Other assembly processes that may contribute to spheroid formation, such as monolithic collapse or quasar-induced expansion (e.g., Fan et al. 2008), have not been considered here and merit future study. Cosmological simulations exploring two-phase assembly predict that up to 80 percent of the stellar mass present in $z = 0$ ETGs has been accreted (Oser et al. 2010). Consequently, kinematical and chemical transitions such as those observed here should be ubiquitous.

Chapter 4

Insights from Simulations

4.1 Introduction

A galaxy's six dimensional phase space structure is a ledger of past interactions and mergers. However, it is currently impossible to obtain such detailed spatial and kinematic information for individual stars in extragalactic systems. Instead, we rely on the integrated velocity distribution of many stars along our line-of-sight (i.e., the LOSVD) and the discrete velocities of bright tracers (e.g., GCs and PNe) projected into two spatial dimensions (see chapters 2 & 3). In this chapter, we discuss techniques for "observing" high-resolution cosmological simulations in order to make direct comparisons with our wide-field kinematic data - the ultimate goal being to progress our understanding of ETG stellar halo assembly.

The canonical view of ETG formation is that their spheroids originate as a consequence of violent relaxation accompanying the chaotic merging of galaxies. Many numerical simulations of binary major-mergers of disk galaxies (e.g., Hernquist 1992, Barnes 1992, Bendo & Barnes 2000, Burkert & Naab 2003, Bournaud et al. 2005, Cox et al. 2006, Hoffman et al. 2010, Chilingarian et al. 2010, Bois et al. 2011) have shown that such interactions create remnants with

similar properties to real world ellipticals and S0s. For instance, these simulations can reasonably reproduce isophote shape (Naab et al. 1999) and kinematic structure within $1\,R_e$ (Jesseit et al. 2007). Given the multiple tunable merger parameters (e.g., mass ratio, gas content, orbital trajectory), much of the diversity of observed ETG features is reproducible (e.g., Bournaud et al. 2005, Cox et al. 2006, Hoffman et al. 2010).

However, alternate theories for ETG bulge formation are gaining popularity given observations of massive turbulent star-forming disks at $z \sim 2$ that appear to be actively forming bulges (Genzel et al. 2006). These disks are thought to be fed by cold streams of gas that flow along cosmological filaments, leading to massive star forming clumps that migrate inwards, disrupt, and form an inner bulge (e.g., Noguchi 1999, Elmegreen et al. 2008, Dekel et al. 2009).

Additionally, views for the origin of extended stellar halos around galaxies have also rapidly changed, with increasing evidence for the dramatic size evolution of massive ETGs between $z \approx 2$–3 and today. ETG bulges appear to gradually grow in size over time (van Dokkum et al. 2010), the implication being that minor mergers and accretion events are responsible for growing their extended stellar halos (Bezanson et al. 2009). This inside-out formation scenario suggests that ETG spheroids are composed of an inner bulge, made of stars formed in-situ, and an ex-situ halo comprised mostly of accreted stars (Naab et al. 2007, Oser et al. 2010).

Whether the in-situ bulge formed as a result of a dissipative major-merger or a fragmenting turbulent disk, the expectation is for a relatively oblate and rotating inner component. The ATLAS^{3D} survey galaxies are consistent with this expectation, with 86% of ETGs exhibiting rapid rotation within $1\,R_e$ (Emsellem et al. 2011). Interestingly, early efforts to probe the kinematic structure of ETGs at larger radius found more diversity, with inner-fast rotators sometimes being outer slow rotators (Proctor et al. 2009, Coccato et al. 2009, Arnold et al. 2011). This implies that inner and outer spheroids can be somewhat decoupled in otherwise well-aligned regular fast rotator ETGs; a feature that jibes with the general expectations of an

inside-out assembly process.

Specifically, expectations for large scale rotational behavior are quite different between major-merger and inside-out formation scenarios. Disk-disk major-merger remnants are generally expected to have rapid outer rotation resulting from residual disk spin and the conversion of orbital into internal angular momentum (e.g., Bendo & Barnes 2000, Cretton et al. 2001). Conversely, a stellar spheroid created from the aggregate accretion of numerous satellites with random orbital trajectories produces a halo with little rotational support (Vitvitska et al. 2002, Abadi et al. 2006, Bournaud et al. 2007).

In this chapter, we compare our wide-field kinematic data to simulated galaxies formed as the result of (i) idealized binary major-mergers and through (ii) the two-phase assembly processes described above.

4.2 Mock Observations of Simulated Galaxies

We analyze the high resolution (70 pc) zoom-in hydrodynamic cosmological simulations described in Ceverino et al. (2010). These simulations are unique in having high enough resolution to resolve the fragmentation of turbulent star-forming disks at high-redshift, while also including a realistic cosmological accretion history. The Ceverino simulations provide six-dimensional phase space information, mass, age, and metallicity values for nearly two million stellar particles. To compare these data with simulations requires projection into two spatial and one velocity dimension. Figure 4.1 shows an illustrative diagram of the overall process.

4.2.1 Measuring half-mass radius

In Chapter 2 we presented spatially resolved two-dimensional kinematics for 22 ETGs. Importantly, the spatial dimensions were normalized by effective or half-light radius in order to

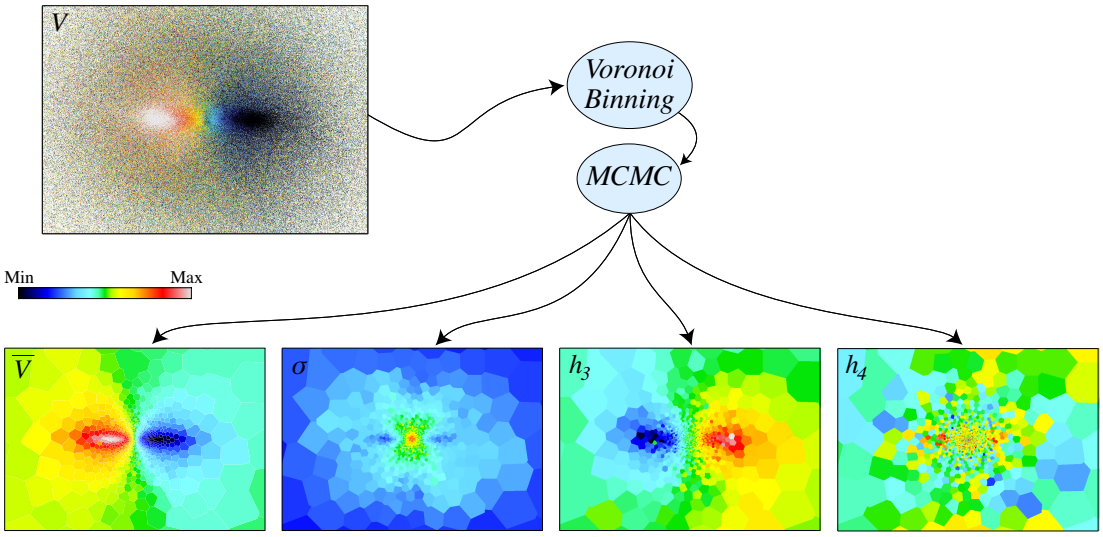

Figure 4.1: Observing simulated galaxies using Voronoi binning and Markov-Chain Monte-Carlo (MCMC) methods. This diagram illustrates the kinematic data derived from simulated galaxies. The top-left panel plots the position of each stellar particle, and colors each particle according to its velocity. These particles are subdivided into Voronoi bins, which are visible as colored polygons in the bottom row of panels. The LOSVD of stellar particle velocities in each Voronoi bin is analyzed using a MCMC method to derive best-fitting parameter values (V, σ, h_3, h_4) and the posterior distributions of their uncertainties.

account for the relatively wide range of ETG sizes ($R_e \approx 1{-}10$ kpc). For the simulated galaxies we use half-mass radius, as a proxy for half-light radius, defined here as the projected circular radius enclosing half the stellar mass.

A complicating issue with computing half-mass radius in cosmological simulations is the presence of substructure and merging satellites. To identify and separate the main bound structures in each simulation, we use the K-means clustering algorithm. Briefly, given an input number K, the algorithm subdivides the stellar particles into K clusters using an iterative cluster centroiding technique. Very small values of K will result in poor separation between clusters, resulting in multiple galaxies per cluster. Conversely, high K values will over-segment the data, leading to unphysical divisions of galaxies into multiple clusters.

We use a simple metric that identifies the optimum number of clusters for each simulation snapshot. Our chosen criteria selects K such that the squared residual distances between particles and their respective cluster centroids are minimized, while the separation between cluster centroids is simultaneously maximized. The cluster with the largest number of stellar particles is taken as the primary galaxy in each simulation snapshot.

In practice we found that clustering using only the three-dimensional spatial positions produced better results than with all six dimensions of phase space information. In principle, a better way to separate the main bound structures would be to use a physical measure of connectedness, such as binding energy. However, accurately computing this quantity for each stellar particle requires a full accounting of the mass in each simulated remnant, including dark matter and gas, which we did not have access to. Furthermore, the adopted spatial clustering method was sufficient for separating the main galaxy remnant from the other large bound structures.

The next step involves rotating the simulation data into a particular viewing angle (e.g., edge-on), and projecting the measurements into two-dimensions. Because we are interested in

rotation, we typically rotate the data such that the resultant angular momentum vector is perpendicular to our line-of-sight. To accomplish this, we measure the net angular momentum vector of all the stellar particles within some limiting radius (typically 2-5 kpc). The simulated remnant is then rotated so the resultant angular momentum vector is along the chosen principal axis. New projected coordinates and line-of-sight velocities are determined for each stellar particle, followed by calculation of the primary galaxy's projected half-mass radius.

4.2.2 Creating LOSVDs

At this stage, we want to convert the catalog of discrete LOS velocity measurements into typical measures of spatially resolved kinematics such as mean velocity V, velocity dispersion σ, h_3, and h_4. Since these quantities describe the shapes of velocity distributions, the measurements must first be binned together to create those distributions. One approach would be to subdivide the projected dataset into a two-dimensional grid of square bins. Some number of stellar particles will fall into each bin, thus creating a distribution of velocities and allowing the above Gauss-Hermite parameters to be measured. However, just as in a real galaxy, the surface density of stellar particles rapidly declines with radius, leading to nearly empty bins at large projected galactocentric radius and extremely populous bins at small radius. Instead, we use a Voronoi binning code (Cappellari & Copin 2003) to subdivide the stellar particles into a series of polygonal Voronoi bins that each contain roughly equal numbers of particles. This approach naturally increases bin sizes with radius to account for the falling density of points, while also allowing fine spatial sampling in high density regions.

In practice, we ignore the assignment of stellar particles to each bin and instead only keep the bin centroids. We use these values to construct a Delaunay triangulation and a new set of polygonal Voronoi bins with known vertices. This extra step is necessary because it allows us to accurately measure the area of each Voronoi bin, and thus compute area normalized quantities

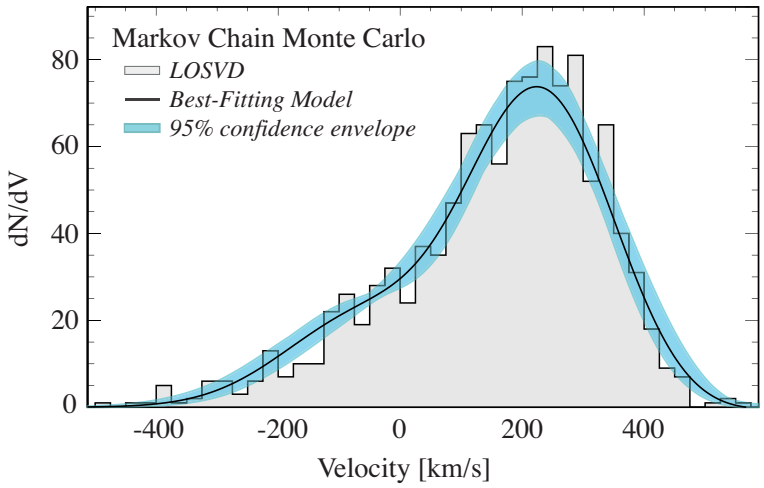

Figure 4.2: MCMC LOSVD fitting results for a single Voronoi bin in Figure 4.1. The distribution of line-of-sight velocities is shown as a filled grey histogram. The truncated Gauss-Hermite series with the highest likelihood is overlaid as a solid black line. The cyan envelope shows the 95% confidence interval of parameter uncertainties, which are determined from the posterior distribution of fitting solutions.

such as mass surface density. Subsequently, each stellar particle is assigned to the Voronoi bin it resides within.

With several hundred stars per bin we can accurately characterize the shape of the LOSVD as a truncated Gauss-Hermite series. We use an affine invariant Bayesian Markov-Chain Monte-Carlo method (Goodman & Weare 2010) to find the best-fitting parameter values and measure the full posterior of parameter uncertainties. Similarly to the regularization scheme adopted in `pPXF`, we impose priors on h_3 and h_4 that helps guard against spurious measurements of these higher order moments. A fiducial LOSVD, most-likely parameterized fit, and envelope of posterior parameter values are shown in Figure 4.2.

4.3 Results and Discussion

Figure 4.3 compares large scale kinematics for an edge-on major-merger, real data for NGC 3377, and a cosmological simulation. The dataset for NGC 3377 includes the integrated stellar light measurements discussed in chapter 2 in addition to large-radius discrete velocity measurements of globular clusters (Pota et al. 2013) and planetary nebulae (Coccato et al. 2009). The major-merger simulation (3:1 mass-ratio; Johansson et al. 2009) shows the expected large scale rotation, with a modest decline in rotation between 3 and 7 R_e. In contrast, NGC 3377 rotates rapidly only within 1 R_e, having a slowly rotating outer spheroid. This is similar to the cosmological simulation which still has a disky inner bulge that also transitions to a slowly rotating outer spheroid. The implication is that a major-merger is an extremely poor fit to the real data, while the cosmological simulation naturally reproduces the large-scale rotational structure of NGC 3377.

An alternative way to produce a fast rotating inner disky structure is via disk regrowth at a relatively recent epoch. Indeed, some ETGs do have steep age and metallicity gradients at small radius that may suggest such a formation scenario. However, the slow rotation in the outer spheroid is telling in and of itself. Regardless of the kinematic behavior in the inner regions, the outer spheroid should rapidly rotate if a major-merger was responsible for forming it. Alternatively, a slowly rotating outer spheroid is naturally expected from an accretionary origin from the collective action of many minor-mergers (Vitvitska et al. 2002, Abadi et al. 2006, Bournaud et al. 2007).

To illustrate this point more clearly, we separate stars from the cosmological simulation into in-situ and ex-situ components, and look at their kinematic structure in the final remnant. In Figure 4.4, we show the rotational behavior of stars formed within 5 kpc, and stars formed beyond 10 kpc. This should effectively separate stars that formed within the main galaxy and

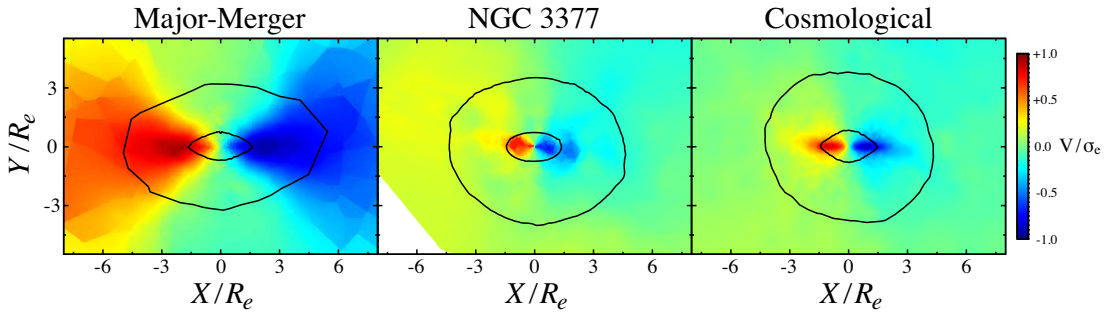

Figure 4.3: Comparison of large-scale rotational patterns from observation and theory. Each panel shows mean velocity normalized by σ_e, the flux weighted root mean square velocity within one effective radius. Left: Residual disk spin and the conversion of orbital into internal angular momentum in binary major-mergers produces remnants with large scale rotational patterns. Middle: The observed wide-field structure of NGC 3377 reveals rapid rotation inside of $1\,R_e$, and slow rotation outside. Right: High resolution cosmological simulations exhibit rapidly rotating in-situ bulges and thick disks and slowly rotating extended outer halos created from disrupted merging satellites. Clearly, the wide-field rotational behavior of NGC 3377 is better matched by a simulated ETG formed in a cosmological simulation with a realistic accretion history.

those formed within satellites. The in-situ stars exhibit a lot of rotation and are arranged in a disky structure as is evident by the diskyness of the $1\,R_e$ isophote. Conversely, the ex-situ stars rotate far less rapidly, though they do rotate and are aligned with the in-situ stars. However, beyond about 2 kpc there is very little rotation. Finally, the $1\,R_e$ isophote for the accreted stars is significantly larger and rounder than for the in-situ stars, demonstrating the extendedness of the ex-situ component.

A similar decoupling between inner and outer kinematic behavior is exhibited by several of the ETGs shown in Chapter 2. Interestingly, two galaxies in our sample that show no rotational decline within $\sim 3\,R_e$ (NGC 1023, 3115), both show large-radius rotational declines (Noordermeer et al. 2008, Coccato et al. 2009, Arnold et al. 2011; see chapter 3;) in their PNe and GC systems. This further highlights the need for large-scale kinematic data in understanding the global structure of ETG halos.

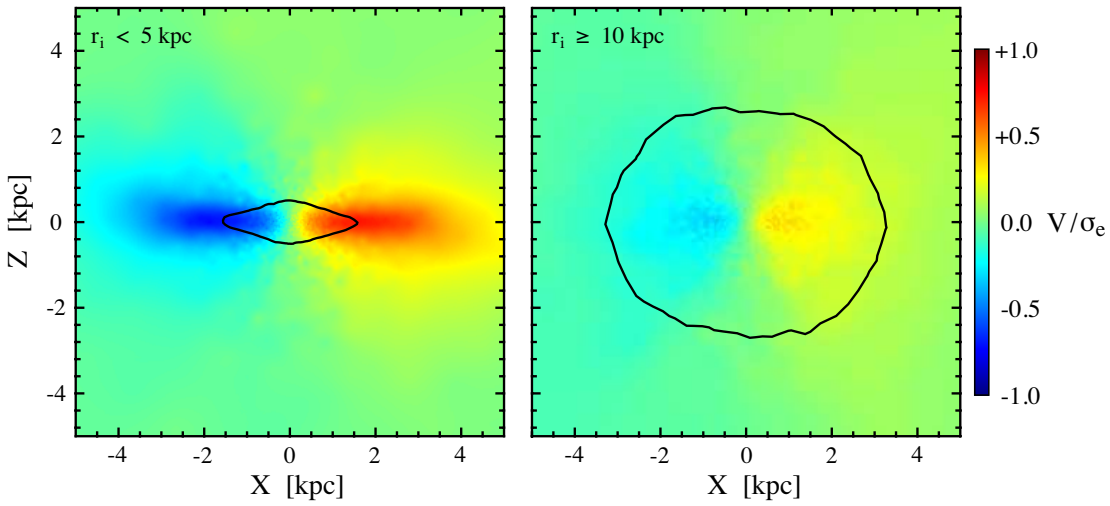

Figure 4.4: Smoothed maps of in-situ and accreted star rotational behavior. Coloring reflects rotational amplitude, and solid black lines denote the half-mass radius of the selected stellar populations. In-situ stars, selected as stellar particles formed at initial radii within 5 kpc of the center of the galaxy, exhibit rapid rotation (left) in the cosmological simulations. Conversely, accreted stars, selected as having formed at galactocentric radii of 10 kpc or greater, show weak aligned rotation (right).

Chapter 5

Summary

The mass-assembly processes responsible for the growth of early-type galaxy stellar halos over the past ~ 10 Gyr have left subtle kinematic and structural clues, particularly at large radius. The longer relaxation times better preserve the formational clues evident in the kinematic properties of integrated stellar light and bright tracer populations such as globular clusters and planetary nebulae. However, obtaining wide-field kinematics for a statistically significant number of galaxies beyond the local group is both observationally challenging and time consuming.

Fortunately, the advent of 10 meter class telescopes and precision wide-field multiplexing spectrographs such as DEIMOS have made these measurements feasible in the last decade. We have utilized these tools to undertake two simultaneous large-scale kinematic surveys of ETGs in the local universe (D<30 Mpc). The data in this thesis represent some of the major data products from these two surveys, and will serve as a landmark dataset for the study of ETG stellar halos for years to come.

Our ongoing survey SMEAGOL (Spectroscopic Mapping of Early-type Galaxies to their Outer Limits) extends spatially resolved integrated-light spectroscopy to $\sim 3\,R_e$. Chapter 2

presents and examines these data for 22 ETGs using a novel smoothing algorithm that uses the spatial correlation of the kinematic measurements to optimally smooth the data. We find that embedded disky structures are common in fast rotator ETGs on these size scales, and are seemingly well-aligned with their encompassing spheroids.

The SAGES Legacy Unifying Globulars and Galaxies Survey (SLUGGS) uses the chemical and kinematic properties of globular clusters to characterize the very large scale structure ($5-10\,R_e$) of ETG halos. In chapter 3, we used these data for the nearby ($\approx$ 9 Mpc) S0 NGC 3115 to constrain its mass assembly history. This galaxy's GC system exhibits a rapid decline in rotation beyond $\approx 3\,R_e$ in addition to a radial decline in metallicity. Taken together, these features suggest that the stellar halo was built primarily through accretion.

Chapter 4 includes some initial comparisons between our large-scale kinematic data and high-resolution cosmological simulations of ETG formation. We show that the large-scale rotation resulting from binary major-mergers does not match the large-radius observations of NGC 3377's stellar halo. However, inclusion of a realistic accretion history in the cosmological simulations leads to galaxy stellar halos with properties that closely match observations.

The previously held views of early-type galaxies as simple featureless systems with straightforward internal structures and assembly histories are becoming increasingly dated. A wealth of new observations of their complex chemical, kinematic, and dynamical structures is helping to reveal the true complexity of these systems. Understanding the formational pathways behind the growth of ETG stellar halos is a critical piece of the puzzle; this thesis represents an important step forward on this path in presenting a detailed large-scale view of the kinematic structure of ETGs.

Bibliography

Abadi, M. G., Navarro, J. F., & Steinmetz, M. 2006, MNRAS, **365**, 747

Arnold, J. A., Romanowsky, A. J., Brodie, J. P., Chomiuk, L., Spitler, L. R., Strader, J., Benson, A. J., & Forbes, D. A. 2011, ApJ, **736**, L26

Ashman, K. M., Bird, C. M., & Zepf, S. E. 1994, AJ, **108**, 2348

Barnes, J. E. 1992, ApJ, **393**, 484

Barth, A. J., Ho, L. C., & Sargent, W. L. W. 2002, AJ, **124(5)**, 2607

Bender, R. 1990, Astronomy and Astrophysics, **229**, 441

Bender, R., Doebereiner, S., & Moellenhoff, C. 1987, Astronomy and Astrophysics, **177**, L53

Bender, R., Saglia, R. P., & Gerhard, O. E. 1994, MNRAS, **269**, 785

Bender, R., Surma, P., Doebereiner, S., Moellenhoff, C., & Madejsky, R. 1989, Astronomy and Astrophysics, **217**, 35

Bendo, G. J. & Barnes, J. E. 2000, MNRAS, **316**, 315

Bezanson, R., Dokkum, P. G. v., Tal, T., Marchesini, D., Kriek, M., Franx, M., & Coppi, P. 2009, ApJ, **697**, 1290

Blakeslee, J. P., Cantiello, M., Mei, S., Côté, P., DeGraaff, R. B., Ferrarese, L., Jordán, A., Peng, E. W., Tonry, J. L., & Worthey, G. 2010, ApJ, **724(1)**, 657

Bois, M., Emsellem, E., Bournaud, F., Alatalo, K., Blitz, L., Bureau, M., Cappellari, M., Davies, R. L., Davis, T. A., de Zeeuw, P. T., Duc, P.-A., Khochfar, S., Krajnović, D., Kuntschner, H., Lablanche, P.-Y., McDermid, R. M., Morganti, R., Naab, T., Oosterloo, T., Sarzi, M., Scott, N., Serra, P., Weijmans, A.-M., & Young, L. M. 2011, MNRAS, **416**, 1654

Bournaud, F., Jog, C. J., & Combes, F. 2005, A&A, **437**, 69

Bournaud, F., Jog, C. J., & Combes, F. 2007, A&A, **476**, 1179

Brodie, J. P. & Strader, J. 2006, arXiv, **(1)**, 193

Buitrago, F., Trujillo, I., Conselice, C. J., Bouwens, R. J., Dickinson, M., & Yan, H. 2008, ApJ, **687**, L61

Burkert, A. & Naab, T. 2003, Galaxies and Chaos, **626**, 327

Capaccioli, M., Held, E. V., & Nieto, J.-L. 1987, AJ, **94**, 1519

Cappellari, M. & Copin, Y. 2003, MNRAS, **342**, 345

Cappellari, M. & Emsellem, E. 2004, PASP, **116**, 138

Cappellari, M., Emsellem, E., Bacon, R., Bureau, M., Davies, R. L., de Zeeuw, P. T., Falcón-Barroso, J., Krajnović, D., Kuntschner, H., McDermid, R. M., Peletier, R. F., Sarzi, M., van den Bosch, R. C. E., & van de Ven, G. 2007, MNRAS, **379**, 418

Cappellari, M., Emsellem, E., Krajnović, D., McDermid, R. M., Scott, N., Verdoes Kleijn, G. A., Young, L. M., Alatalo, K., Bacon, R., Blitz, L., Bois, M., Bournaud, F., Bureau, M., Davies, R. L., Davis, T. A., de Zeeuw, P. T., Duc, P.-A., Khochfar, S., Kuntschner, H., Lablanche,

P.-Y., Morganti, R., Naab, T., Oosterloo, T., Sarzi, M., Serra, P., & Weijmans, A.-M. 2011, MNRAS, **413(2)**, 813

Cenarro, A. J., Cardiel, N., Gorgas, J., Peletier, R. F., Vazdekis, A., & Prada, F. 2001, ApJ, **326(3)**, 959

Ceverino, D., Dekel, A., & Bournaud, F. 2010, MNRAS, **404**, 2151

Chilingarian, I. V., Di Matteo, P., Combes, F., Melchior, A. L., & Semelin, B. 2010, ApJ, **518**, A61

Cimatti, A., Cassata, P., Pozzetti, L., Kurk, J., Mignoli, M., Renzini, A., Daddi, E., Bolzonella, M., Brusa, M., Rodighiero, G., Dickinson, M., Franceschini, A., Zamorani, G., Berta, S., Rosati, P., & Halliday, C. 2008, A&A, **482**, 21

Coccato, L., Gerhard, O., & Arnaboldi, M. 2010, ApJ, **407(1)**, L26

Coccato, L., Gerhard, O., Arnaboldi, M., Das, P., Douglas, N. G., Kuijken, K., Merrifield, M. R., Napolitano, N. R., Noordermeer, E., Romanowsky, A. J., Capaccioli, M., Cortesi, A., de Lorenzi, F., & Freeman, K. C. 2009, MNRAS, **394**, 1249

Cooper, M. C., Newman, J. A., Davis, M., Finkbeiner, D. P., & Gerke, B. F. 2012, Astrophysics Source Code Library, **-1**, 03003

Cortesi, A., Merrifield, M. R., Arnaboldi, M., Gerhard, O., Martinez-Valpuesta, I., Saha, K., Coccato, L., Bamford, S., Napolitano, N. R., Das, P., Douglas, N. G., Romanowsky, A. J., Kuijken, K., Capaccioli, M., & Freeman, K. C. 2011, ApJ, **414(1)**, 642

Cox, T. J., Dutta, S. N., Di Matteo, T., Hernquist, L., Hopkins, P. F., Robertson, B., & Springel, V. 2006, ApJ, **650**, 791

Cretton, N., Naab, T., Rix, H.-W., & Burkert, A. 2001, ApJ, **554**, 291

Daddi, E., Renzini, A., Pirzkal, N., Cimatti, A., Malhotra, S., Stiavelli, M., Xu, C., Pasquali, A., Rhoads, J. E., Brusa, M., di Serego Alighieri, S., Ferguson, H. C., Koekemoer, A. M., Moustakas, L. A., Panagia, N., & Windhorst, R. A. 2005, ApJ, **626**, 680

Davies, R. L., Efstathiou, G., Fall, S. M., Illingworth, G., & Schechter, P. L. 1983, ApJ, **266**, 41

Debattista, V. P., Maria Corsini, E., & Aguerri, J. A. L. 2002, ApJ, **332(1)**, 65

Dekel, A., Sari, R., & Ceverino, D. 2009, ApJ, **703**, 785

Djorgovski, S. & Davis, M. 1987, ApJ, **313**, 59

Dokkum, P. G. v., Franx, M., Kriek, M., Holden, B., Illingworth, G. D., Magee, D., Bouwens, R., Marchesini, D., Quadri, R., Rudnick, G., Taylor, E. N., & Toft, S. 2008, ApJ, **677**, L5

Dressler, A., Lynden-Bell, D., Burstein, D., Davies, R. L., Faber, S. M., Terlevich, R., & Wegner, G. 1987, ApJ, **313**, 42

Elmegreen, B. G., Bournaud, F., & Elmegreen, D. M. 2008, ApJ, **688**, 67

Emsellem, E., Cappellari, M., Krajnović, D., Alatalo, K., Blitz, L., Bois, M., Bournaud, F., Bureau, M., Davies, R. L., Davis, T. A., de Zeeuw, P. T., Khochfar, S., Kuntschner, H., Lablanche, P.-Y., McDermid, R. M., Morganti, R., Naab, T., Oosterloo, T., Sarzi, M., Scott, N., Serra, P., van de Ven, G., Weijmans, A.-M., & Young, L. M. 2011, MNRAS, **414**, 888

Emsellem, E., Cappellari, M., Krajnović, D., van de Ven, G., Bacon, R., Bureau, M., Davies, R. L., de Zeeuw, P. T., Falcón-Barroso, J., Kuntschner, H., McDermid, R., Peletier, R. F., & Sarzi, M. 2007, MNRAS, **379**, 401

Emsellem, E., Cappellari, M., Peletier, R. F., McDermid, R. M., Bacon, R., Bureau, M., Copin,

Y., Davies, R. L., Krajnović, D., Kuntschner, H., Miller, B. W., & de Zeeuw, P. T. 2004, MNRAS, **352**, 721

Faber, S. M. 2003, in Instrument Design and Performance for Optical/Infrared Ground-based Telescopes, pp 1657–1669, SPIE

Fabricius, M. H., Saglia, R. P., Fisher, D. B., Drory, N., Bender, R., & Hopp, U. 2012, ApJ, **754(1)**, 67

Fan, L., Lapi, A., de Zotti, G., & Danese, L. 2008, ApJ, **689**, L101

Forbes, D. A. & Bridges, T. 2010, MNRAS, **404**, 1203

Forbes, D. A., Spitler, L. R., Strader, J., Romanowsky, A. J., Brodie, J. P., & Foster, C. 2011, MNRAS, p. 306

Forestell, A. D. & Gebhardt, K. 2010, ApJ, **716(1)**, 370

Foster, C., Spitler, L. R., Romanowsky, A. J., Forbes, D. A., Pota, V., Bekki, K., Strader, J., Proctor, R. N., Arnold, J. A., & Brodie, J. P. 2011, MNRAS, **415**, 3393

Gebhardt, K., Richstone, D., Tremaine, S., Lauer, T. R., Bender, R., Bower, G., Dressler, A., Faber, S. M., Filippenko, A. V., Green, R., Grillmair, C., Ho, L. C., Kormendy, J., Magorrian, J., & Pinkney, J. 2003, ApJ, **583**, 92

Genzel, R., Tacconi, L. J., Eisenhauer, F., Förster Schreiber, N. M., Cimatti, A., Daddi, E., Bouché, N., Davies, R., Lehnert, M. D., Lutz, D., Nesvadba, N., Verma, A., Abuter, R., Shapiro, K., Sternberg, A., Renzini, A., Kong, X., Arimoto, N., & Mignoli, M. 2006, Nature, **442(7104)**, 786

Gerhard, O. E. 1993, ApJ, **265**, 213

Goodman, J. & Weare, J. 2010, CAMCoS, **5(1)**, 65

Harris, W. E. 2009, ApJ, **703**, 939

Hernquist, L. 1992, ApJ, **400**, 460

Hoffman, L., Cox, T. J., Dutta, S., & Hernquist, L. 2010, ApJ, **723**, 818

Hopkins, P. F., Cox, T. J., Dutta, S. N., Hernquist, L., Kormendy, J., & Lauer, T. R. 2009, The Astrophysical Journal Supplement, **181**, 135

Illingworth, G. 1977, ApJ, **218**, L43

Illingworth, G. & Schechter, P. L. 1982, ApJ, **256**, 481

Jarrett, T. H., Chester, T., Cutri, R., Schneider, S., Skrutskie, M., & Huchra, J. P. 2000, AJ, **119(5)**, 2498

Jesseit, R., Naab, T., Peletier, R. F., & Burkert, A. 2007, MNRAS, **376**, 997

Johansson, P. H., Naab, T., & Burkert, A. 2009, ApJ, **690**, 802

Khochfar, S., Emsellem, E., Serra, P., Bois, M., Alatalo, K., Bacon, R., Blitz, L., Bournaud, F., Bureau, M., Cappellari, M., Davies, R. L., Davis, T. A., de Zeeuw, P. T., Duc, P.-A., Krajnović, D., Kuntschner, H., Lablanche, P.-Y., McDermid, R. M., Morganti, R., Naab, T., Oosterloo, T., Sarzi, M., Scott, N., Weijmans, A.-M., & Young, L. M. 2011, MNRAS, **417**, 845

Kormendy, J. & Bender, R. 1996, ApJ, **464**, L119

Kormendy, J., Fisher, D. B., Cornell, M. E., & Bender, R. 2009, ApJ, **182(1)**, 216

Krajnovic, D., Alatalo, K., Blitz, L., Bois, M., Bournaud, F., Bureau, M., Cappellari, M., Davies, R. L., Davis, T. A., de Zeeuw, P. T., Duc, P.-A., Emsellem, E., Khochfar, S., Kuntschner,

H., McDermid, R. M., Morganti, R., Naab, T., Oosterloo, T., Sarzi, M., Scott, N., Serra, P., Weijmans, A. M., & Young, L. M. 2012, MNRAS

Krajnović, D., Bacon, R., Cappellari, M., Davies, R. L., de Zeeuw, P. T., Emsellem, E., Falcón-Barroso, J., Kuntschner, H., McDermid, R. M., Peletier, R. F., Sarzi, M., van den Bosch, R. C. E., & van de Ven, G. 2008, MNRAS, **390**, 93

Krajnović, D., Cappellari, M., de Zeeuw, P. T., & Copin, Y. 2006, MNRAS, **366**, 787

Krajnović, D., Emsellem, E., Cappellari, M., Alatalo, K., Blitz, L., Bois, M., Bournaud, F., Bureau, M., Davies, R. L., Davis, T. A., de Zeeuw, P. T., Khochfar, S., Kuntschner, H., Lablanche, P.-Y., McDermid, R. M., Morganti, R., Naab, T., Oosterloo, T., Sarzi, M., Scott, N., Serra, P., Weijmans, A.-M., & Young, L. M. 2011, MNRAS, **414**, 2923

Kronawitter, A., Saglia, R. P., Gerhard, O., & Bender, R. 2000, A&A, **144**, 53

Kundu, A. & Whitmore, B. C. 2001, AJ, **122**, 1251

Kuntschner, H., Ziegler, B. L., Sharples, R. M., Worthey, G., & Fricke, K. J. 2002, A&A, **395**, 761

Lauer, T. R., Ajhar, E. A., Byun, Y. I., Dressler, A., Faber, S. M., Grillmair, C., Kormendy, J., Richstone, D., & Tremaine, S. 1995, AJ, **110**, 2622

Mackey, A. D., Huxor, A. P., Ferguson, A. M. N., Irwin, M. J., Tanvir, N. R., McConnachie, A. W., Ibata, R. A., Chapman, S. C., & Lewis, G. F. 2010, ApJ, **717**, L11

Méndez, R. H., Teodorescu, A. M., Kudritzki, R. P., & Burkert, A. 2009, ApJ, **691(1)**, 228

Méndez, R. H., Thomas, D., Saglia, R. P., Maraston, C., Kudritzki, R. P., & Bender, R. 2005, ApJ, **627(2)**, 767

Murphy, J. D., Gebhardt, K., & Adams, J. J. 2011, ApJ, **729(2)**, 129

Naab, T. & Burkert, A. 2001, ApJ, **555**, L91

Naab, T., Burkert, A., & Hernquist, L. 1999, ApJ, **523**, L133

Naab, T., Jesseit, R., & Burkert, A. 2006, MNRAS, **372**, 839

Naab, T., Johansson, P. H., & Ostriker, J. P. 2009, ApJ, **699**, L178

Naab, T., Johansson, P. H., Ostriker, J. P., & Efstathiou, G. 2007, ApJ, **658**, 710

Newman, A. B., Ellis, R. S., Bundy, K., & Treu, T. 2012, ApJ, **746(2)**, 162

Nieto, J.-L., Bender, R., & Surma, P. 1991, Astronomy and Astrophysics, **244**, L37

Noguchi, M. 1999, ApJ, **514**, 77

Noordermeer, E., Merrifield, M. R., Coccato, L., Arnaboldi, M., Capaccioli, M., Douglas, N. G., Freeman, K. C., Gerhard, O., Kuijken, K., de Lorenzi, F., Napolitano, N. R., & Romanowsky, A. J. 2008, MNRAS, **384**, 943

Norris, M. A., Sharples, R. M., Bridges, T., Gebhardt, K., Forbes, D. A., Proctor, R., Raul Faifer, F., Carlos Forte, J., Beasley, M. A., Zepf, S. E., & Hanes, D. A. 2008, MNRAS, **385**, 40

Norris, M. A., Sharples, R. M., & Kuntschner, H. 2006, MNRAS, **367**, 815

Oser, L., Naab, T., Ostriker, J. P., & Johansson, P. H. 2011, AJ, **744(1)**, 63

Oser, L., Ostriker, J. P., Naab, T., Johansson, P. H., & Burkert, A. 2010, ApJ, **725**, 2312

Peng, E. W., Ford, H. C., & Freeman, K. C. 2004, ApJ, **602**, 685

Peng, E. W., Jordán, A., Côté, P., Blakeslee, J. P., Ferrarese, L., Mei, S., West, M. J., Merritt, D., Milosavljević, M., & Tonry, J. L. 2006, ApJ, **639**, 95

Peng, E. W., Jordán, A., Côté, P., Takamiya, M., West, M. J., Blakeslee, J. P., Chen, C.-W., Ferrarese, L., Mei, S., Tonry, J. L., & West, A. A. 2008, ApJ, **681**, 197

Pinkney, J., Gebhardt, K., Bender, R., Bower, G., Dressler, A., Faber, S. M., Filippenko, A. V., Green, R., Ho, L. C., Kormendy, J., Lauer, T. R., Magorrian, J., Richstone, D., & Tremaine, S. 2003, ApJ, **596**, 903

Pota, V., Forbes, D. A., Romanowsky, A. J., Brodie, J. P., Spitler, L. R., Strader, J., Foster, C., Arnold, J. A., Benson, A., Blom, C., Hargis, J. R., Rhode, K. L., & Usher, C. 2013, MNRAS, **428(1)**, 389

Proctor, R. N., Forbes, D. A., Forestell, A., & Gebhardt, K. 2005, MNRAS, **362**, 857

Proctor, R. N., Forbes, D. A., Romanowsky, A. J., Brodie, J. P., Strader, J., Spolaor, M., Mendel, J. T., & Spitler, L. 2009, MNRAS, **398**, 91

Pu, S. B., Saglia, R. P., Fabricius, M. H., Thomas, J., Bender, R., & Han, Z. 2010, Astronomy and Astrophysics, **516**, 4

Puzia, T. H., Kissler-Patig, M., Thomas, D., Maraston, C., Saglia, R. P., Bender, R., Richtler, T., Goudfrooij, P., & Hempel, M. 2004, A&A, **415**, 123

Puzia, T. H. & Sharina, M. E. 2008, ApJ, **674**, 909

Rix, H.-W. & White, S. D. M. 1990, ApJ, **362**, 52

Sánchez-Blázquez, P., Peletier, R. F., Jiménez-Vicente, J., Cardiel, N., Cenarro, A. J., Falcón-Barroso, J., Gorgas, J., Selam, S., & Vazdekis, A. 2006, MNRAS, **371**, 703

Scorza, C. & Bender, R. 1995, A&A, **293**, 20

Searle, L. & Zinn, R. 1978, ApJ, **225**, 357

Spolaor, M., Forbes, D. A., Hau, G. K. T., Proctor, R. N., & Brough, S. 2008, MNRAS, **385(2)**, 667

Statler, T. S. & Smecker-Hane, T. 1999, AJ, **117(2)**, 839

Stewart, K. R., Bullock, J. S., Wechsler, R. H., Maller, A. H., & Zentner, A. R. 2008, ApJ, **683**, 597

Tonry, J. L., Dressler, A., Blakeslee, J. P., Ajhar, E. A., Fletcher, A. B., Luppino, G. A., Metzger, M. R., & Moore, C. B. 2001, ApJ, **546(2)**, 681

Trujillo, I., Förster Schreiber, N. M., Rudnick, G., Barden, M., Franx, M., Rix, H.-W., Caldwell, J. A. R., McIntosh, D. H., Toft, S., Häussler, B., Zirm, A., Dokkum, P. G. v., Labbé, I., Moorwood, A., Röttgering, H., van der Wel, A., van der Werf, P., & van Starkenburg, L. 2006, ApJ, **650**, 18

van der Marel, R. P. 1991, MNRAS, **253**, 710

van der Marel, R. P. & Franx, M. 1993, ApJ, **407**, 525

van Dokkum, P. G., Whitaker, K. E., Brammer, G., Franx, M., Kriek, M., Labbé, I., Marchesini, D., Quadri, R., Bezanson, R., Illingworth, G. D., Muzzin, A., Rudnick, G., Tal, T., & Wake, D. 2010, AJ, **709(2)**, 1018

Vazdekis, A., Sánchez-Blázquez, P., Falcón-Barroso, J., Cenarro, A. J., Beasley, M. A., Cardiel, N., Gorgas, J., & Peletier, R. F. 2010, MNRAS, **404**, 1639

Vitvitska, M., Klypin, A. A., Kravtsov, A. V., Wechsler, R. H., Primack, J. R., & Bullock, J. S. 2002, ApJ, **581**, 799

Weijmans, A.-M., Cappellari, M., Bacon, R., de Zeeuw, P. T., Emsellem, E., Falcón-Barroso, J., Kuntschner, H., McDermid, R. M., van den Bosch, R. C. E., & van de Ven, G. 2009, MNRAS, **398**, 561

White, S. D. M. 1980, Royal Astronomical Society, **191**, 1P

White, S. D. M. & Rees, M. J. 1978, MNRAS, **183**, 341

Wuyts, S., Cox, T. J., Hayward, C. C., Franx, M., Hernquist, L., Hopkins, P. F., Jonsson, P., & van Dokkum, P. G. 2010, ApJ, **722(2)**, 1666

Zolotov, A., Willman, B., Brooks, A. M., Governato, F., Brook, C. B., Hogg, D. W., Quinn, T., & Stinson, G. 2009, ApJ, **702**, 1058